

AD-A159 015

EFFECT OF TEMPERATURE AND STRAIN RATE ON MICROSTRUCTURE
OF A DEFORMED SUPERPLASTIC AL-10ZMG-01ZNR ALLOY(U)
NAVAL POSTGRADUATE SCHOOL MONTEREY CA D B BERTHOLD

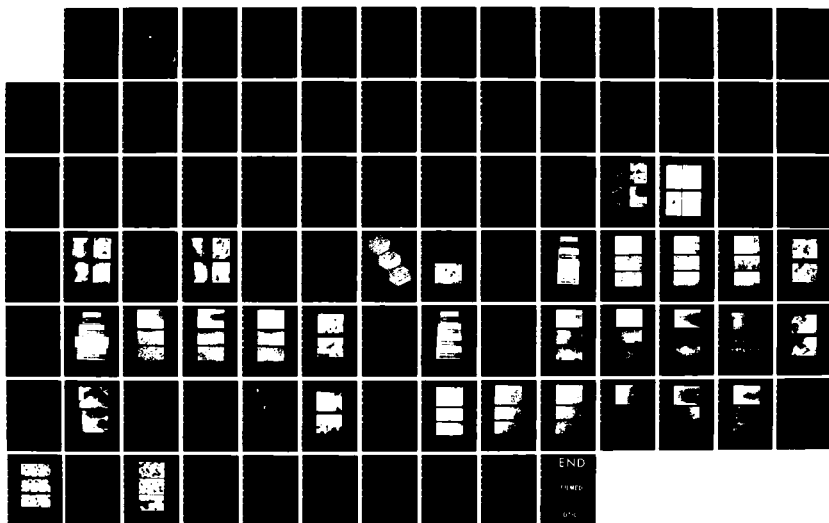
1/1

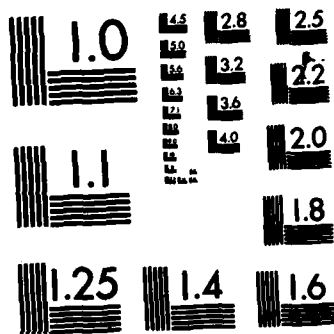
UNCLASSIFIED

JUN 85

F/G 11/6

NL





MICROCOPY RESOLUTION TEST CHART
NATIONAL BUREAU OF STANDARDS-1963-A

NAVAL POSTGRADUATE SCHOOL

Monterey, California

AD-A159 015



THESIS

EFFECT OF TEMPERATURE AND STRAIN RATE
ON MICROSTRUCTURE OF A DEFORMED,
SUPERPLASTIC Al-10%Mg-0.1%Zr ALLOY

by

Dudley B. Berthold
June 1985

Thesis Advisor:

T. R. McNelley

DTIC
EXECTE
SEP 13 1985

DTIC FILE COPY

Approved for public release; distribution is unlimited

REPORT DOCUMENTATION PAGE		READ INSTRUCTIONS BEFORE COMPLETING FORM
1. REPORT NUMBER	2. GOVT ACCESSION NO. AD-A159	3. RECIPIENT'S CATALOG NUMBER 015
4. TITLE (and Subtitle) EFFECT OF TEMPERATURE AND STRAIN RATE ON MICROSTRUCTURE OF A DEFORMED SUPERPLASTIC Al-10%Mg-0.1%Zr ALLOY		5. TYPE OF REPORT & PERIOD COVERED Master's Thesis; June 1985
		6. PERFORMING ORG. REPORT NUMBER
7. AUTHOR(s) Dudley B. Berthold		8. CONTRACT OR GRANT NUMBER(s)
9. PERFORMING ORGANIZATION NAME AND ADDRESS Naval Postgraduate School Monterey, California 93943-5100		10. PROGRAM ELEMENT, PROJECT, TASK AREA & WORK UNIT NUMBERS
11. CONTROLLING OFFICE NAME AND ADDRESS Naval Postgraduate School Monterey, California 93943-5100		12. REPORT DATE June 1985
		13. NUMBER OF PAGES 90
14. MONITORING AGENCY NAME & ADDRESS (if different from Controlling Office)		15. SECURITY CLASS. (of this report) Unclassified
		15a. DECLASSIFICATION/DOWNGRADING SCHEDULE
16. DISTRIBUTION STATEMENT (of this Report) Approved for public release; distribution is unlimited		
17. DISTRIBUTION STATEMENT (of the abstract entered in Block 20, if different from Report)		Accession For NTIS GRA&I <input checked="" type="checkbox"/> DTIC TAB <input type="checkbox"/> Unannounced <input type="checkbox"/> Justification
		By Distribution/
18. SUPPLEMENTARY NOTES		Availability Codes Avail and/or Dist Special
		AL
19. KEY WORDS (Continue on reverse side if necessary and identify by block number) Superplasticity, Aluminum, Aluminum Alloys, Aluminum-Magnesium, Thermomechanical Processing, Dynamic Recrystallizations, Cavitation		
20. ABSTRACT (Continue on reverse side if necessary and identify by block number) Development of microstructure during thermomechanical processing of an Al-10%Mg-0.1%Zr alloy was examined in the initial portion of this research. The thermomechanical processing involved solution treating, hot working by upset forging at 440°C followed by warm rolling at 300°C to a 94% reduction. Subsequently, test specimens from this rolled material were deformed at three strain rates at temperatures		

20. (Continued)

of 200°C, 300°C, and 400°C and were microstructurally examined. It is found that this alloy statically recrystallizes prior to commencing a test at 400°C, the resultant grains deform by boundary sliding and there is extensive cavitation. During lower temperature deformation it was found that either continuous recrystallization or just recovery with no recrystallization occurs and little or no cavitation takes place.

Approved for public release; distribution is unlimited

Effect of Temperature and Strain Rate
on Microstructure of a Deformed,
Superplastic Al-10%Mg-0.1%Zr Alloy

by

Dudley B. Berthold
Lieutenant, United States Navy
B.A., University of Louisville, 1978


Submitted in partial fulfillment of the
requirements for the degree of

MASTER OF SCIENCE IN MECHANICAL ENGINEERING

from the

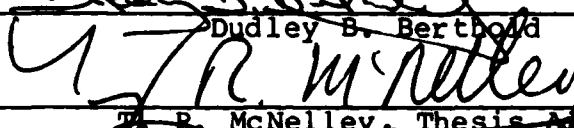
NAVAL POSTGRADUATE SCHOOL
June 1985

Author:

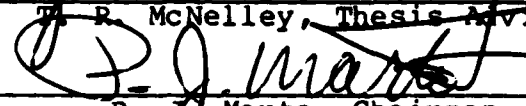


Dudley B. Berthold

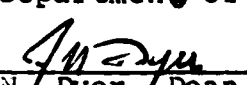
Approved by:



T. R. McNelley, Thesis Advisor



P. J. Marto, Chairman,
Department of Mechanical Engineering



John N. Dyer, Dean of Science and Engineering

ABSTRACT

Development of microstructure during thermomechanical processing of an Al-10%Mg-0.1%Zr alloy was examined in the initial portion of this research. The thermomechanical processing involved solution treating, hot working by upset forging at 440°C followed by warm rolling at 300°C to a 94% reduction. Subsequently, test specimens from this rolled material were deformed at three strain rates at temperatures of 200°C, 300°C, and 400°C and were microstructurally examined. It is found that this alloy statically recrystallizes prior to commencing a test at 400°C, the resultant grains deform by boundary sliding and there is extensive cavitation. During lower temperature deformation it was found that either continuous recrystallization or just recovery with no recrystallization occurs and little or no cavitation takes place.

TABLE OF CONTENTS

I.	INTRODUCTION	12
II.	BACKGROUND	16
A.	SUPERPLASTIC BEHAVIOR	16
1.	General Prerequisites	16
2.	Strain Rate Sensitivity	16
3.	Deformation Mechanisms	17
4.	Microstructural Characteristics	23
5.	Activation Energy	24
B.	PREVIOUS WORK AT THE NAVAL POSTGRADUATE SCHOOL	25
III.	EXPERIMENTAL PROCEDURES	28
A.	MATERIAL PROCESSING	28
B.	TENSILE SPECIMEN FABRICATION	30
C.	ANNEALING	32
D.	METALLOGRAPHY	33
IV.	RESULTS AND DISCUSSION	35
A.	EVOLUTION OF MICROSTRUCTURE DURING THERMOMECHANICAL PROCESSING	35
1.	As-Cast Microstructure	35
2.	Solution-Treated Microstructure	38
3.	Upset-Forged Microstructure	42
4.	Warm-Rolled Microstructure	42
B.	MICROSTRUCTURAL EXAMINATION OF AS-ROLLED TEST SPECIMENS	48

1. Specimens Tested at 200 °C	48
2. Specimens Tested at 300 °C	54
3. Specimens Tested at 400 °C	60
C. MICROSTRUCTURAL EXAMINATION OF RECRYSTALLIZED TEST SPECIMENS	71
1. Recrystallization Treatment	71
2. Specimens Tested at 300 °C	74
3. Specimens Tested at 400 °C	74
D. MICROSTRUCTURAL EXAMINATION OF ANNEALED TEST SPECIMENS	81
1. Annealing Treatment	81
2. Specimens Tested at 300 °C	81
V. CONCLUSION AND RECOMMENDATION	85
LIST OF REFERENCES	87
INITIAL DISTRIBUTION LIST	90

LIST OF FIGURES

1.1	Partial aluminum-magnesium phase diagram	14
2.1	Nabarro-Herring vacancy flow model	18
2.2	Ashby-Verrall grain boundary sliding model	21
3.1	Thermomechanical processing scheme	29
3.	Stages of processing	31
3.3	Test specimen dimensions	32
4.1	Optical micrographs of the as-cast micro- structure of an Al-10%Mg-0.1%Zr alloy: (a) and (b) show $ZrAl_3$ particles (denoted by arrows) in center of grains with heavy Mg_5Al_8 precipitate on grain boundaries; (c) and (d) are polarized light micrographs showing dendritic segregation	36
4.2	In (a) a $ZrAl_3$ particle is shown in a deformed test specimen; (b) is an energy dispersive map of the particle; (c) shows the energy-dispersive X-Ray spectrum of the particle and (d) shows the energy-dispersive X-Ray spectrum of the surrounding matrix	37
4.3	Partial aluminum-zirconium phase diagram	39
4.4	Optical micrographs of an Al-10%Mg-0.1%Zr alloy solution treated 24 hours at 440°C and then oil quenched: (a) and (b) show $ZrAl_3$ particles (denoted by arrows) present as before and (c) and (d) are polarized light micrographs showing a much more homogeneous structure	41
4.5	Optical micrographs of an Al-10%Mg-0.1%Zr alloy solution treated 24 hours at 440°C, up-set forged, annealed 1 hour at 440°C and oil quenched: (a) and (b) show $ZrAl_3$ particles (denoted by arrows) present as before and (c) and (d) are polarized light micrographs showing an even more homogeneous structure	43

4.6	The increase in hardness and the precipitation of Mg from solution during warm rolling. Data from McNelley and Garg [Ref. 31]	45
4.7	Tri-planar micrographs of an Al-10%Mg-0.1%Zr alloy warm rolled at 300°C to three different strains: (a) $\epsilon \approx .55$, (b) $\epsilon \approx .77$, and (c) $\epsilon \approx .91$	46
4.8	TEM micrograph of an Al-10%Mg-0.1%Zr alloy warm rolled at 300°C and air cooled to room temperature	47
4.9	Photographs of 200°C test specimens: (a) untested, (b) deformed to fracture at $\dot{\epsilon} = 6.67 \times 10^{-2} \text{s}^{-1}$, elongation 70%, (c) deformed to fracture at $\dot{\epsilon} = 6.67 \times 10^{-3} \text{s}^{-1}$, elongation 107%, and (d) deformed to fracture at $\dot{\epsilon} = 6.67 \times 10^{-4} \text{s}^{-1}$, elongation 127%	49
4.10	Optical micrographs of a test specimen deformed to fracture at 100°C and $\dot{\epsilon} = 6.67 \times 10^{-2} \text{s}^{-1}$: (a) fracture point, (b) gage section and (c) grip section	50
4.11	Optical micrographs of a test specimen deformed to fracture at 100°C and $\dot{\epsilon} = 6.67 \times 10^{-3} \text{s}^{-1}$: (a) fracture point, (b) gage section and (c) grip section	51
4.12	Optical micrographs of a test specimen deformed to fracture at 100°C and $\dot{\epsilon} = 6.67 \times 10^{-4} \text{s}^{-1}$: (a) fracture point, (b) gage section and (c) grip section	52
4.13	TEM micrographs of 200°C test specimen: (a) deformed to fracture at $\dot{\epsilon} = 6.67 \times 10^{-3} \text{s}^{-1}$ and (b) deformed to fracture at $\dot{\epsilon} = 6.67 \times 10^{-4} \text{s}^{-1}$	53
4.14	Photographs of 300°C test specimens: (a) untested, (b) deformed to fracture at $\dot{\epsilon} = 6.67 \times 10^{-2} \text{s}^{-1}$, elongation 221%, (c) deformed to fracture at $\dot{\epsilon} = 6.67 \times 10^{-3} \text{s}^{-1}$, elongation 480%, and (d) deformed to fracture at $\dot{\epsilon} = 6.67 \times 10^{-4} \text{s}^{-1}$, elongation 330%	55
4.15	Optical micrographs of a test specimen deformed to fracture at 300°C and $\dot{\epsilon} = 6.67 \times 10^{-2} \text{s}^{-1}$: (a) fracture point, (b) gage section and (c) grip section	56

4.16	Optical micrographs of a test specimen deformed to fracture at 300 °C and $\dot{\epsilon} = 6.67 \times 10^{-3} \text{s}^{-1}$: (a) fracture point, (b) gage section and (c) grip section	57
4.17	Optical micrographs of a test specimen deformed to fracture at 300 °C and $\dot{\epsilon} = 6.67 \times 10^{-4} \text{s}^{-1}$: (a) fracture point, (b) gage section and (c) grip section	58
4.18	TEM micrographs of 300 °C test specimen: (a) deformed to fracture at $\dot{\epsilon} = 6.67 \times 10^{-3} \text{s}^{-1}$ and (b) deformed to fracture at $\dot{\epsilon} = 6.67 \times 10^{-4} \text{s}^{-1}$	59
4.19	Photographs of 400 °C test specimens: (a) untested, (b) deformed to fracture at $\dot{\epsilon} = 6.67 \times 10^{-2} \text{s}^{-1}$, elongation 168%, (c) deformed to fracture at $\dot{\epsilon} = 6.67 \times 10^{-3} \text{s}^{-1}$, elongation 204%, and (d) deformed to fracture at $\dot{\epsilon} = 6.67 \times 10^{-4} \text{s}^{-1}$, elongation 222%	61
4.20	Optical micrographs of a test specimen deformed to fracture at 400 °C and $\dot{\epsilon} = 6.67 \times 10^{-2} \text{s}^{-1}$: (a) fracture point, (b) gage section and (c) grip section	63
4.21	Optical micrographs of a test specimen deformed to fracture at 400 °C and $\dot{\epsilon} = 6.67 \times 10^{-3} \text{s}^{-1}$: (a) fracture point, (b) gage section and (c) grip section	64
4.22	Optical micrographs of a test specimen deformed to fracture at 400 °C and $\dot{\epsilon} = 6.67 \times 10^{-4} \text{s}^{-1}$: (a) fracture point, (b) gage section and (c) grip section	65
4.23	Optical micrographs showing ZrAl_3 particles present within cavity stringers in a test specimen deformed at 400 °C	66
4.24	TEM micrographs of 400 °C test specimen; (a) deformed to fracture at $\dot{\epsilon} = 6.67 \times 10^{-3} \text{s}^{-1}$ and (b) deformed to fracture at $\dot{\epsilon} = 6.67 \times 10^{-4} \text{s}^{-1}$	67
4.25	TEM micrographs showing dislocation arrangement into a subgrain configuration	69
4.26	True stress at 0.1 strain vs. temperature for test specimens in the as-rolled condition	70

4.27	Optical Micrographs of specimens annealed at 440°C for (a) 30 sec; (b) 60 sec; (c) 5 minute and (d) 30 minutes	72
4.28	TEM micrograph of a recrystallized test specimen before deformation	73
4.29	Optical micrographs of a recrystallized test specimen deformed at 300°C and $\dot{\epsilon} = 6.67 \times 10^{-2} \text{s}^{-1}$: (a) fracture point, (b) gage section and (c) grip section	75
4.30	Optical micrographs of a recrystallized test specimen deformed at 300°C and $\dot{\epsilon} = 6.67 \times 10^{-3} \text{s}^{-1}$: (a) fracture point, (b) gage section and (c) grip section	76
4.31	Optical micrographs of a recrystallized test specimen deformed at 300°C and $\dot{\epsilon} = 6.67 \times 10^{-4} \text{s}^{-1}$: (a) fracture point, (b) gage section and (c) grip section	77
4.32	Optical micrographs of a recrystallized test specimen deformed at 400°C and $\dot{\epsilon} = 6.67 \times 10^{-2} \text{s}^{-1}$: (a) fracture point, (b) gage section and (c) grip section	78
4.33	Optical micrographs of a recrystallized test specimen deformed at 400°C and $\dot{\epsilon} = 6.67 \times 10^{-3} \text{s}^{-1}$: (a) fracture point, (b) gage section and (c) grip section	79
4.34	Optical micrographs of a recrystallized test specimen deformed at 400°C and $\dot{\epsilon} = 6.67 \times 10^{-4} \text{s}^{-1}$: (a) fracture point, (b) gage section and (c) grip section	80
4.35	TEM micrographs of Al-10%Mg-0.1%Zr alloy in warm rolled condition annealed at 200°C for times: (a) as-rolled, (b) 1 hour and (c) 10 hours	82
4.36	TEM micrographs of annealed test specimens deformed to fracture at 300°C: (a) $\dot{\epsilon} = 6.67 \times 10^{-3} \text{s}^{-1}$; (b) $\dot{\epsilon} = 6.67 \times 10^{-4} \text{s}^{-1}$, and (c) $\dot{\epsilon} = 6.67 \times 10^{-5} \text{s}^{-1}$	84

ACKNOWLEDGEMENT

I would like to thank my advisor, Professor T. R. McNelley and Dr. E. W. Lee for their expert assistance and guidance in conducting this research, the Naval Air Systems Command and Mr. Richard Schmidt for their financial support and continued interest in superplastic aluminum alloys. Finally, I would like to thank my wife, Debbie, and my two children, Bryant and Bridgette, for their love and support during my tour here at the Naval Postgraduate School.

I. INTRODUCTION

In recent years there has been an increased interest in superplastic aluminum alloys. This interest has arisen because of the many opportunities for application that these materials possess. These opportunities include: (1) ease of shaping material components (i.e., vacuum forming methods employed in the plastics industry could be utilized in the metal industry); (2) high strength components of complicated geometry could be formed, where previously fasteners and/or welding were required; (3) structural components requiring a combination of high strength, good ductility, and light weight could be produced.

Superplastic alloys in general have elongations to failure of two hundred percent or more under appropriate conditions of temperature and rate of deformation. Although the mechanical properties for many alloys and the conditions under which superplasticity occur are well known, the mechanisms of such behavior are not yet fully understood.

The purpose of this research is to establish some of the basic microstructure-mechanical property relationships associated in a superplastic Al-10%Mg-0.1%Zr alloy. The high magnesium content was chosen as a result of previous research work at the Naval Postgraduate School [Ref. 1-12]. This previous research has shown that thermomechanically

processed high-magnesium alloys exhibit high strength with good ductility at ambient temperatures. The essential features of the thermomechanical processing include:

- (1) solution treatment to dissolve all soluble components, especially the magnesium;
- (2) hot working to refine and further homogenize the microstructure;
- (3) quenching from the solution treatment/hot working temperature;
- (4) reheating and warm working to large strains;
- (5) air cooling to ambient temperature.

The zirconium addition was made in an attempt to minimize grain growth. Fine $ZrAl_3$ particles act as excellent grain boundary pinners [Ref. 13], resulting in a fine grain size which is considered essential for superplastic behavior.

Conventional aluminum-magnesium alloys may develop microstructures susceptible to stress corrosion cracking. Here, due to the thermomechanical processing, a homogeneous dispersion of beta (Mg_5Al_8) is formed vice a grain boundary dispersion. Hence, a magnesium content as high as 10 percent can be used vice the 5-6 percent in conventional alloys.

In general, there are several reasons that magnesium is used as a primary alloying element. The two most predominate include: (1) magnesium has good solubility in solution (see Figure 1.1) and although precipitation does occur in aluminum-magnesium alloys, much of its strength is due to magnesium in solution and (2) magnesium is less dense than

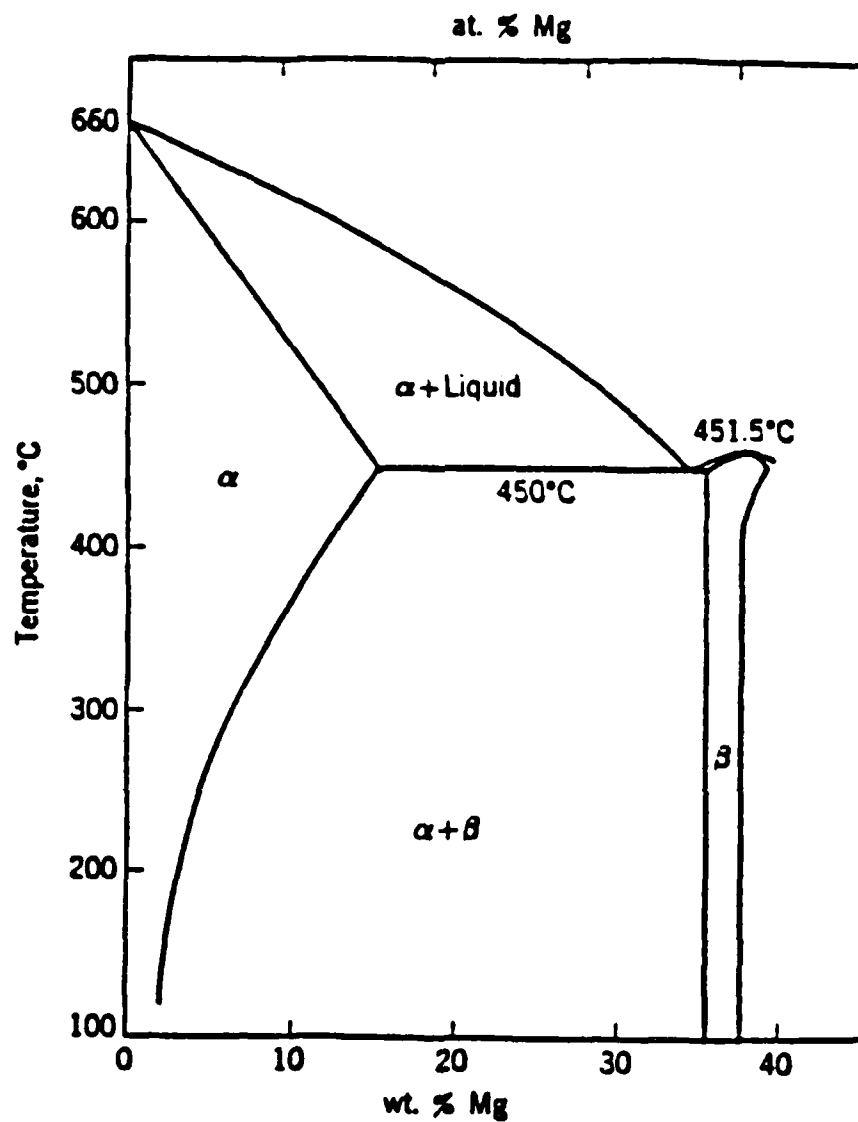


Figure 1.1 Partial aluminum-magnesium phase diagram

pure aluminum and its addition results in a weight savings. These factors coupled with superplasticity may provide an appealing combination.

II. BACKGROUND

A. SUPERPLASTIC BEHAVIOR

1. General Prerequisites

Superplasticity is usually considered as the achievement of high tensile elongations (generally in excess of 200 percent). Active research in the field of superplasticity began when Underwood [Ref. 14] published the first English language review of superplasticity in 1962. Since that time several reviews have been published reflecting the increased understanding of the phenomenon. The most commonly agreed upon prerequisites for superplasticity are: (1) fine, equiaxed grain structure with high angle grain boundaries; (2) a deformable second phase, if present; (3) a thermally stable microstructure; (4) elevated temperatures in the range of 0.5-0.7 T_m ; (5) low strain rates; and (6) resistance to cavitation [Ref. 15].

2. Strain Rate Sensitivity

Superplastic behavior is found in materials in which the flow stress is highly strain rate sensitive. In analysis of deformation at elevated temperature, the flow stress (σ) is often related to strain rate ($\dot{\epsilon}$) by a power law relation, equation 2.1:

$$\sigma = K \dot{\epsilon}^m \quad (\text{eqn. 2.1})$$

where K is a microstructure and temperature-dependent material constant and m is referred to as the strain rate sensitivity coefficient, defined as

$$m = \frac{d(\ln \sigma)}{d(\ln \dot{\epsilon})} \quad (\text{eqn. 2.2})$$

i.e., the slope of a plot of stress versus strain rate on logarithmic axes. A large value of m enhances the resistance to the localizing of plastic flow in a neck by causing an increased resistance to further deformation once necking begins to occur. Typical superplastic materials have an m value in the range 0.3-0.7. A high m value alone, however, does not necessarily lead to superplastic behavior since it is only related with resistance to localized necking and does not take into account other failure modes, such as cavitation.

3. Deformation Mechanisms

Over the years a number of theories have been proposed to account for creep data, emphasizing that several mechanisms can be responsible for creep deformation at elevated temperatures. A few of the well accepted models will be reviewed in this section.

Considering deformation at low stresses and high temperatures, Nabarro [Ref. 16] and Herring [Ref. 17] proposed that the creep process was controlled by

stress-directed diffusion. This 'diffusional creep' involves the migration of vacancies along a gradient from grain boundaries experiencing tensile stresses to boundaries undergoing compression; simultaneously atoms would be moving in the opposite direction, resulting in an elongation of grains (see Figure 2.1). Nabarro-Herring creep is described by equation 2.3:

$$\dot{\epsilon}_s = \frac{7 \sigma D_v b^3}{k T d^2} \quad (\text{eqn. 2.3})$$

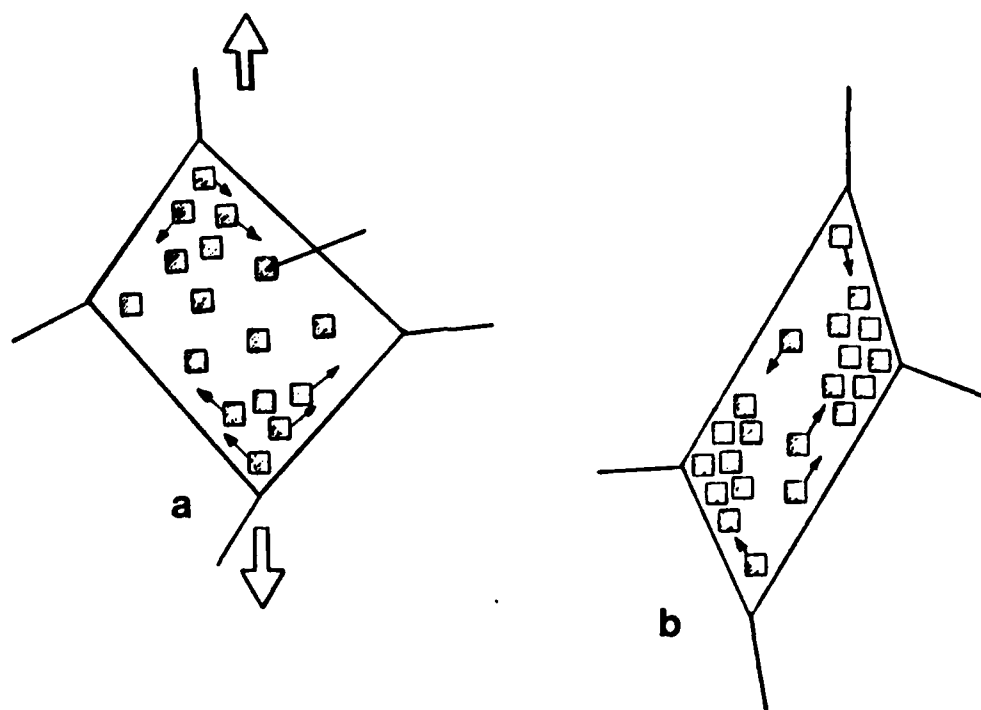


Figure 2.1 Nabarro-Herring vacancy flow model

where $\dot{\epsilon}$ is the steady-state creep rate, k is Boltzmann's constant, T is absolute temperature, D_v is the volume diffusivity, b is the Burger's vector, σ is applied stress and d is the grain size.

Coble [Ref. 18] proposed a closely related mechanism, involving grain boundary diffusion versus lattice diffusion. Coble creep is described by equation 2.4:

$$\dot{\epsilon}_s = \frac{50 \sigma D_b b^4}{k T d^3} \quad (\text{eqn. 2.4})$$

where D_b is boundary diffusivity and all other variables as described before. Ashby [Ref. 19] reanalyzed and combined the Nabarro-Herring and Coble creep models in the form of equation 2.5:

$$\dot{\epsilon} = \frac{14 \sigma b^3 D_v}{k T d^2} \left(1 + \frac{\pi \delta D_b}{d D_v} \right) \quad (\text{eqn. 2.5})$$

where D_v is volume diffusivity, D_b is boundary diffusivity, δ is grain boundary thickness and all other variables as described before. Here, it is essentially assumed that boundary and volume diffusion will contribute to straining in an additive way and hence the faster of the processes described separately by equations 2.3 and 2.4 will be observed.

All the diffusion creep models described above predict that deformation is a diffusion controlled process with either an inverse second power or inverse third power dependence on grain size. These models result in an m -value of one and predict strain rates far below those observed. Additionally, they suggest an increase in the aspect ratio (lengthening in the direction of major tensile strains) which is in conflict with experimental observations of superplastically deformed materials. A diffusional based creep model more consistent with the strain rates and microstructure topological features (equiaxed grains) observed was proposed by Ashby and Verrall [Ref. 20]. This model involves grain boundary sliding accommodated by diffusion (see Figure 2.2). The Ashby-Verrall analysis resulted in the model given by equation 2.6:

$$\dot{\epsilon} = \frac{98b^3 D_v}{kTd^2} \left(\sigma - \frac{0.72\gamma}{d} \right) \left(1 + \frac{\pi\delta D_b}{dD_v} \right) \quad (\text{eqn. 2.6})$$

where all terms have been previously defined except γ , the grain boundary surface energy. As before, the Ashby-Verrall model predicts an inverse grain size dependence. At high temperatures where lattice diffusion is the primary rate controlling process there is an inverse second power dependence on grain size, while at low temperatures where boundary diffusion would be expected as the primary rate

controlling process there is an inverse third power dependence on grain size. Note also that the applied stress has to be of magnitude greater than the threshold term ($0.72\tau/d$) to increase the grain boundary area and attain the intermediate state (middle of Figure 2.2) required for grain boundary sliding.

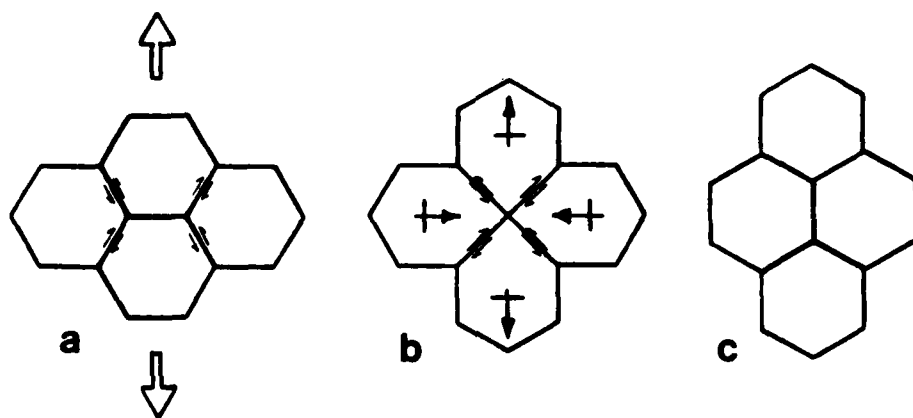


Figure 2.2 Ashby-Verrall grain boundary sliding model

At intermediate to high stresses and high temperatures, creep deformation is believed to be controlled primarily by diffusion assisted movement of the dislocations. The Weertman [Ref. 21] model proposes that creep is controlled by edge dislocation climb away from dislocation obstacles, either by interstitial or vacancy generation or annihilation. These obstacles are assumed to be

Cottrell-Lomer locks, which are formed by dislocation intersection processes. Dislocations are continuously being generated by Frank-Read sources and those overcoming obstacles are thus replaced by others from such sources. Weertman described pure metal creep by equation 2.7:

$$\dot{\epsilon} = A_1 \sigma^{4.5} \exp \left(\frac{-Q_c}{RT} \right) \quad (\text{eqn. 2.7})$$

where A_1 is a constant, Q_c is the activation energy required for edge dislocation climb to occur, R is the gas constant and T is absolute temperature. Noting that creep data for solid solutions was considerably different than that for pure metal behavior he developed another model known as the microcreep theory of Weertman. He showed that when dislocation motion under stress was controlled by velocity of solute drag along with the dislocation line, the creep rate is described by equation 2.8:

$$\dot{\epsilon} = A_2 \sigma^3 \exp \left(\frac{-Q_s}{RT} \right) \quad (\text{eqn. 2.8})$$

where A_2 is a constant and Q_s is the activation energy for solute diffusion. This model predicts that the creep rate of solid solutions should be proportional to the third power of stress in contrast to the 4.5 power law dependence predicted in pure metals [Ref. 22].

4. Microstructural Characteristics

A homogeneous, fine grain size smaller than 10 microns is typical of superplastic materials. This fine grain size is considered a microstructural requirement for superplasticity. It is generally accepted that grain boundary sliding with either diffusional or slip accommodation contribute appreciably to the elongations achieved at low imposed strain rates [Ref. 23]. At higher imposed strain rates, grain boundary sliding and diffusion occur too slowly to contribute appreciably, and so dislocation motion is considered the principle deformation mechanism.

Any of the previously discussed diffusional creep models can be used to illustrate the sensitivity of strain rate to grain size. It is clear that an increase in grain size at a constant strain rate results in an increase in stress. Thus, if grain growth were to occur during a test, the material would strain harden if equation 2.3, 2.4, 2.5 or 2.6 were to describe the rate-stress relationship. To retard grain growth under high temperature test conditions, some form of fine, deformable precipitate is required to act as a grain boundary pinner [Refs. 24 and 25]. This inter-metallic precipitate phase should be similar in strength to the matrix to minimize the formation of cavities [Ref. 26]. Zener and McLean proposed that grain boundaries of growing grains would interact with dispersed particles and become

pinned by them when the retarding force due to the particles balances the driving force due to reduction in surface energy of the grains. From the Zener-McLean relationship described by equation 2.9:

$$d \approx \frac{4r}{3f} \quad (\text{eqn. 2.9})$$

where d is the distance between particles, r is particle radius and f is the volume fraction of particles, it is clear that for a given volume fraction of precipitate, a smaller particle size will result in a finer grain size.

5. Activation Energy

The activation energy (Q), is a measure of the energy required for a temperature-dependent process. The Weertman model discussed previously, for example, shows the explicit relationship for a thermally activated process.

Often, activation energy values for deformation are the same as those for lattice diffusion, suggesting that dislocation climb by lattice diffusion is the controlling process [Ref. 22]. A lower value for activation energy is observed when grain boundary sliding, accommodated by grain boundary diffusion, controls the deformation process. Diffusion in the grain boundaries (the rate controlling process) occurs more readily than diffusion in the grain interior and is characterized by the lower activation energy. Hence, activation energy measurements may provide

useful insight into the mechanisms involved in a super-plastic material.

B. PREVIOUS WORK AT THE NAVAL POSTGRADUATE SCHOOL

Aluminum-magnesium alloys have been the subject of extensive investigation and study at the Naval Postgraduate School. This study was initially pursued in an attempt to obtain an alloy possessing a high-strength to weight ratio along with good corrosion resistance, machinability, ductility, and toughness. More recent research has been focused on the superplastic deformation characteristics of such an alloy.

Investigation of aluminum-magnesium alloys began in 1976 when Ness [Ref. 1] investigated the effect that warm rolling might have on homogenizing the microstructure of an Al-13%Mg alloy. His work demonstrated that a warm rolling process could produce an alloy with a homogeneous microstructure. However, due to cracking during the rolling process, the warm rolling procedure employed was extremely slow and required that only small reductions per pass be made.

Bingay [Ref. 2] and Glover [Ref. 3] concurrently followed Ness's work. Both worked with 15% and 19% magnesium aluminum magnesium alloys. Again cracking during the rolling process was a major problem. Hence, subsequent work was shifted to lower magnesium content alloys.

Grandon [Ref. 4] in his study of 7-10% magnesium aluminum alloys introduced a twenty-four hour solution treatment at 400°C followed by warm rolling at 300°C. He found that these alloys maintained good ductility and high strength. He also noted that recrystallization did not occur during warm rolling at temperatures below the solvus. Speed [Ref. 5] followed Grandon's work with a 12% magnesium aluminum alloy. Speed introduced an isothermal forging process at the twenty hour point of the twenty-four hour solution treatment.

Chesterman [Ref. 6] studied (via optical microscopy) the nature of precipitation and recrystallization in alloys containing a magnesium content of 8-14 percent. He found that recrystallization occurred only at temperatures above the solvus and that precipitation was the method by which stored energy was released when annealing at temperatures below the solvus.

Johnson [Ref. 7] combined all the previous studies and standardized a thermomechanical process for high-magnesium aluminum magnesium alloys. His processing technique included solution treatment for 10 hours at 440°C with a isothermal upset forge at the 9 hour point, followed by an oil quench and warm rolling at temperatures between 200°C and 340°C. He concluded that the beta phase (Mg_5Al_8) intermetallic was a significant factor in obtaining both high strength and good ductility. Shirah [Ref. 9] expanded

upon Johnson's work and found that microstructure homogeneity could be improved by increasing the solution treatment time to 24 hours.

Becker [Ref. 9] developed procedures for isothermal tensile testing at elevated temperatures. His work involved the tensile testing of Al-8%Mg-0.4%Cu and Al-10%Mg-0.5%Mn specimens. He observed superplastic elongations up to 400 percent and noted that the higher magnesium content alloy had better superplastic characteristics.

Mills [Ref. 10] did a comprehensive study on the Al-10%Mg-0.5%Mn alloy previously studied by Becker. He noted that the superplastic ductilities observed at temperatures above the solvus were the result of grain boundary sliding.

Stengel [Ref. 11] studied the effects of different annealing treatments prior to tensile testing. Stengel reported that annealing below the rolling temperature of 300 °C enhanced superplastic behavior.

Self [Ref. 12] investigated the effects that various alloy additions to a high magnesium aluminum magnesium might have on its superplasticity. He noted that the addition of copper or manganese, at the same weight percentage, has the same effect on superplasticity.

III. EXPERIMENTAL PROCEDURES

A. MATERIAL PROCESSING

The alloy selected for investigation was of nominal composition Al-10%Mg-0.1%Zr (composition in weight percent). The alloy was obtained from the Alcoa Technical Center, Alcoa Center, PA, as direct-chill-cast ingot. The alloy was produced utilizing 99.99% pure aluminum as a base metal and alloying was done with commercially pure magnesium and Al-Zr master alloy additions. To further grain refinement in the casting, Ti-B was used and Be was added for oxidation control. Composition details are provided in Table I [Ref. 27].

TABLE I
Alloy Composition (Weight Percent)

Serial Number	Mg	Zr	Si	Fe	Al
57284	9.90	.09	.02	.02	Balance

Billets of dimension 32mm x 32mm x 95mm (1.25 in x 1.25 in x 3.75 in) were sectioned from the as-cast ingot to facilitate subsequent thermomechanical processing. The thermomechanical processing scheme is illustrated in Figure 3.1. To promote a homogeneous material, the billets are solution treated at 440 °C for 24 hours and isothermally upset forged

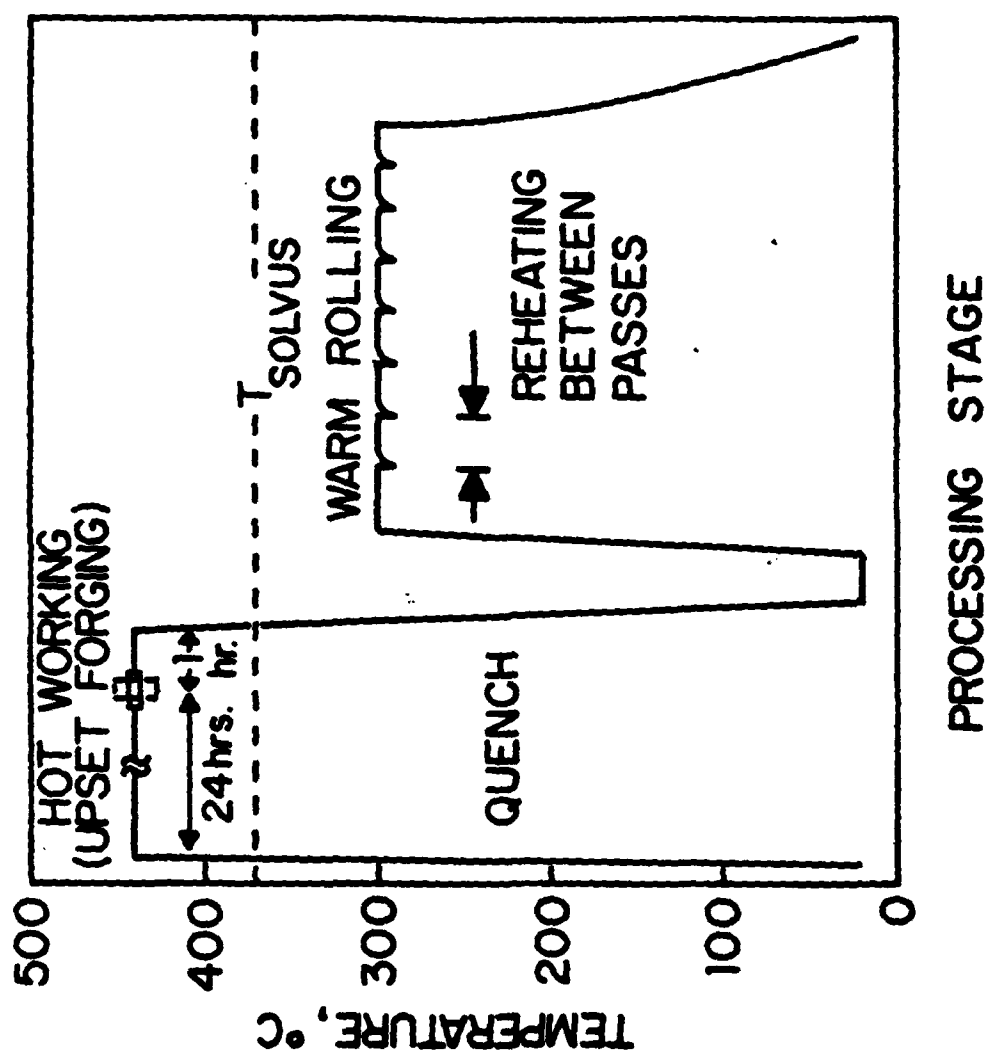


Figure 3.1 Thermomechanical processing scheme

at 440°C utilizing heated platens. Final height was approximately 28mm (1.1in), resulting in a reduction of about 71 percent. After forging the billets were annealed at 440°C for 1 hour and then oil quenched.

The final stage of the processing method entailed rolling the billets into sheets at a temperature of 300°C. To insure an isothermal condition, the billets were placed in an air furnace for 30 minutes prior to the first rolling pass and were reheated for ten-minute intervals between subsequent passes until a final thickness of 2.0mm (0.08in) was obtained. The rolling process required about 22 passes per billet at an approximate 0.762mm (0.03in) reduction in thickness per pass. Figure 3.2 illustrates the different stages of thermomechanical processing and test specimen manufacturing. Further discussion of the processing done on the material of this research is given by Hartman [Ref. 28] and Alcamo [Ref. 29].

B. TENSILE SPECIMEN FABRICATION

Tensile specimens were fabricated from the rolled sheets. Blanks 69.9mm x 19.1mm (.275in x 0.75in) in size were cut on a bandsaw by first removing approximately 76.2mm (3in) from each end and squaring the sides. The test specimens were machined from these blanks by endmilling. Dimensions are shown in Figure 3.3.

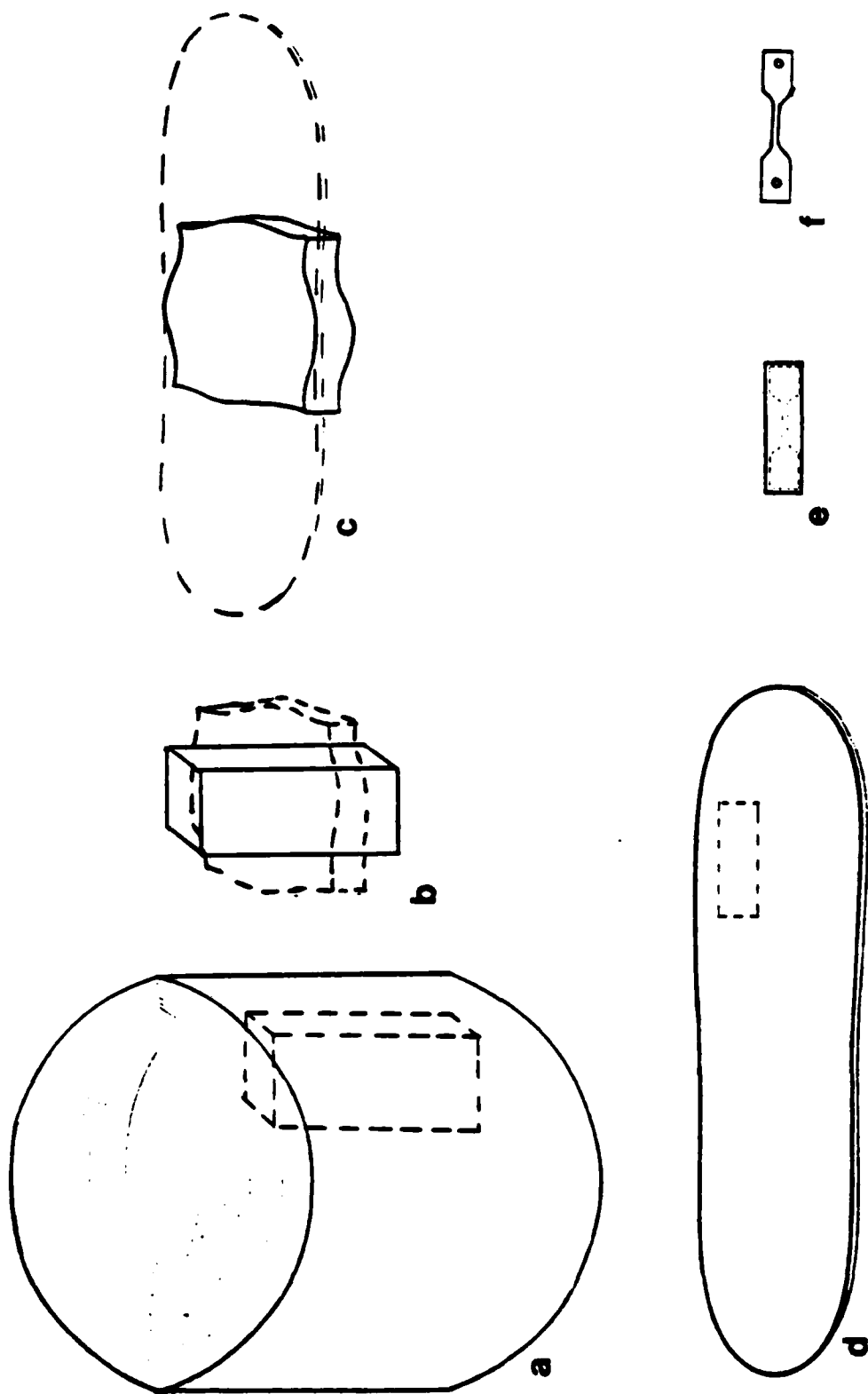


Figure 3.2 Stages of Processing

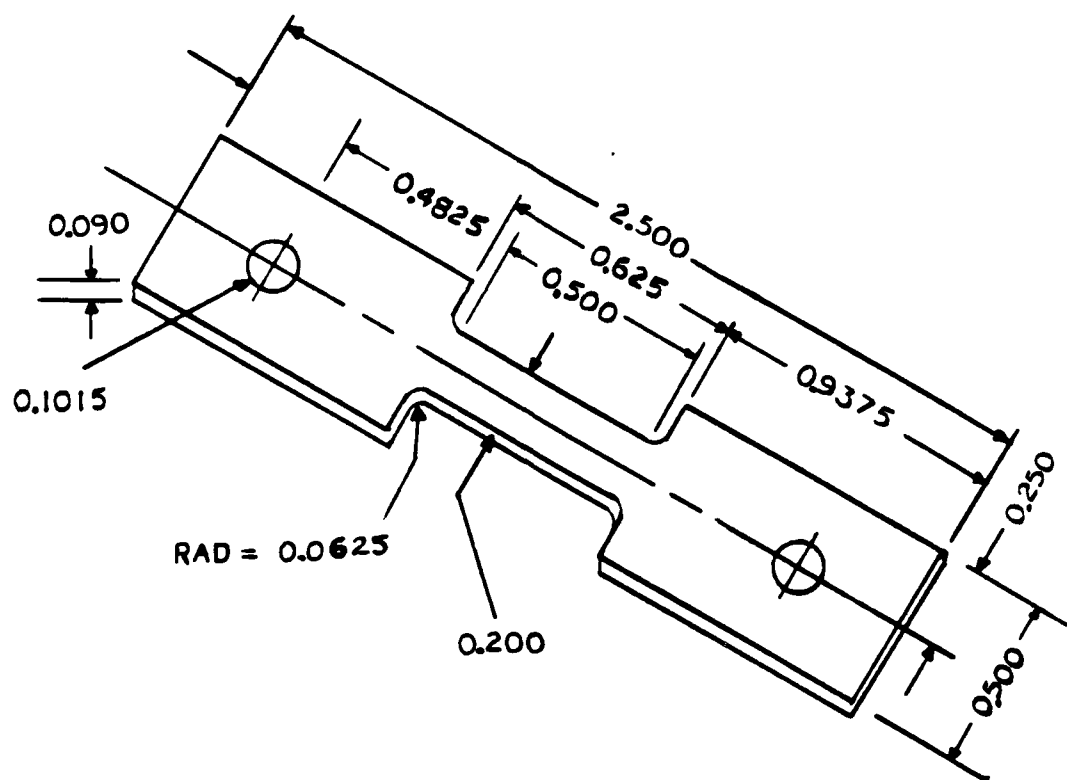


Figure 3.3 Test specimen dimensions

C. ANNEALING

Annealing treatments of 1 hour at 200°C (to induce recovery) and 1 minute at 440°C (to facilitate recrystallization) were utilized in this research. Tensile specimens were annealed in a salt bath comprised of approximately 2 liters of Cal Alloy #3010 Quenching Salt, heated in a Lindberg Type 56622 crucible furnace. Fresh salt was melted and the temperature allowed to stabilize over a 24 hour

period. An omega K-type Chromel-Alumel thermocouple connected to a Newport Laboratories Inc. digital readout was used to monitor temperature.

The annealing technique involved suspending the tensile specimens from a horizontal steel rod by a thin Nichrome wire such that they were completely immersed in the molten salt, yet not touching the sides or bottom of the furnace. Upon completion of the heat treatment the specimens were removed and air cooled to room temperature.

D. METALLOGRAPHY

Both optical and transmission electron microscopy was carried out during this research. The specimens examined included ones from different stages of processing, as well as selected samples from the elevated test specimens tested by Hartman [Ref. 28].

Specimens optically examined were cold mounted with a fast cure acrylic compound using a plastic ring mold sprayed with a silicone mold release. Mounted specimens were polished by first wet sanding with 240 to 600 grit paper and then polishing on a 0.05 micron gamma alumina polishing wheel, followed by a magnesium oxide polishing wheel. The polished specimens were etched either with a Graf-Sargent solution (84ml H₂O, 15.5ml HNO₃, 0.5ml HF, 3g CrO₃) for times varying from 30-90 seconds, or with Barker's reagent (2.5ml HBF₄, 100ml H₂O) at 20 volts d.c. for times varying

from 40-90 seconds. Examination and photographic work was done with a Zeiss Universal microscope. Particles of interest were identified with an energy dispersive method via a PGT-1000 X-Ray emission microanalysis system. Kodak 35mm Technical Pan film was used for optical micrographic recording.

Thin foil specimens for transmission electron microscope observation were prepared by first cutting the specimens to an approximate thickness of 1mm (0.04in). This was accomplished by utilizing a low-concentration wafering blade on a low-speed diamond saw. These cut specimens were further reduced in thickness to approximately 0.25mm (0.001in) by sanding with 600 grit paper. From this thin foil, a 3.0mm (0.12in) disc was punched out. This disc was electrothinned utilizing a Struers Tenupol 2 Electro-Thinning unit set at 12 volt d.c. and utilizing a -20°C solution of 2 parts methyl alcohol to 1 part HNO₃. Examination and photographic work was done with a JEOL JEM-100CX II Electron Microscope. Kodak Electron Microscope Film 4489 was used for micrographic recording.

IV. RESULTS AND DISCUSSION

A. EVOLUTION OF MICROSTRUCTURE DURING THERMOMECHANICAL PROCESSING

1. As-Cast Microstructure

The Al-10%Mg-0.1%Zr alloy used in this study was produced by the direct chill cast method. In direct chill casting, molten metal is poured into the top of a water-cooled copper mold and solid material is withdrawn from the bottom. The bottom end of the mold is initially closed by a water-cooled copper plate and this plate is then lowered as a support for the solidifying alloy. This method provides a relatively high cooling rate which is needed to curtail coring and segregation in the alloy. The resultant microstructure is uniform on a macroscope level but on a microscope scale it is dendritic and thus non-homogeneous.

Figure 4.1 shows micrographs of the as-cast material. The beta precipitate (Mg_5Al_3) is heavily concentrated at the grain boundaries, with very little in the grain interiors. There are also constituent particles located in the centers of many grains. These constituent particles (denoted by arrows in Figure 4.1) were identified as $ZrAl_3$ particles. Figure 4.2 reveals the emitted X-Ray distribution of zirconium for both the particle and the

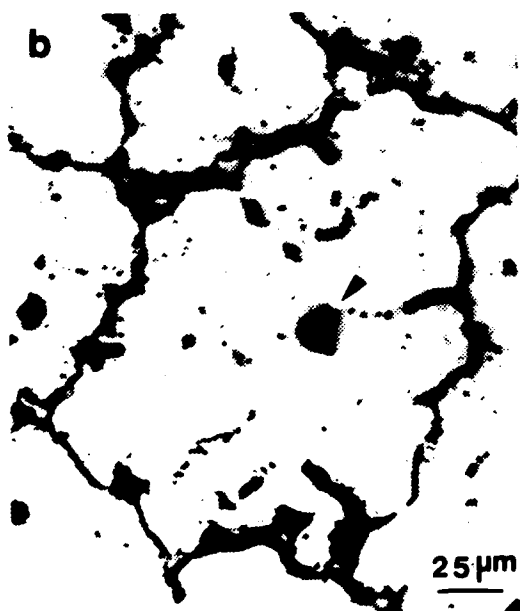
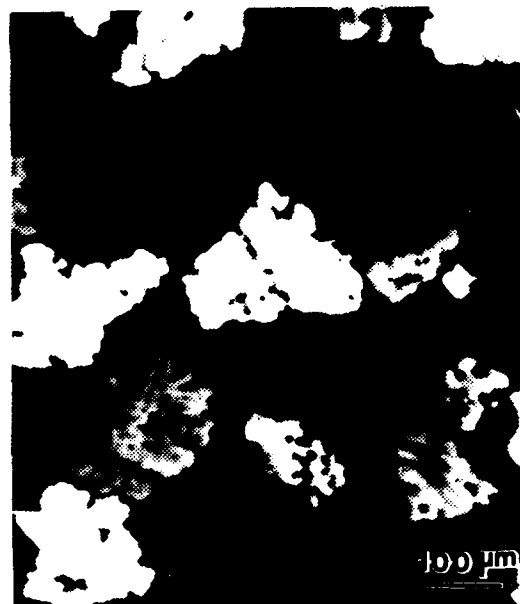
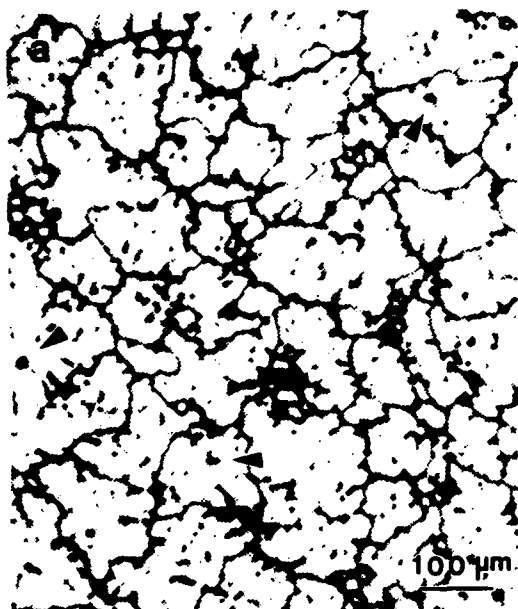


Figure 4.1 Optical micrographs of the as-cast microstructure of an Al-10%Mg-0.1%Zr alloy: (a) and (b) show $ZrAl_3$ particles (denoted by arrows) in center of grains with heavy Mg_5Al_8 precipitated on grain boundaries; (c) and (d) are polarized light micrographs showing dendritic segregation.

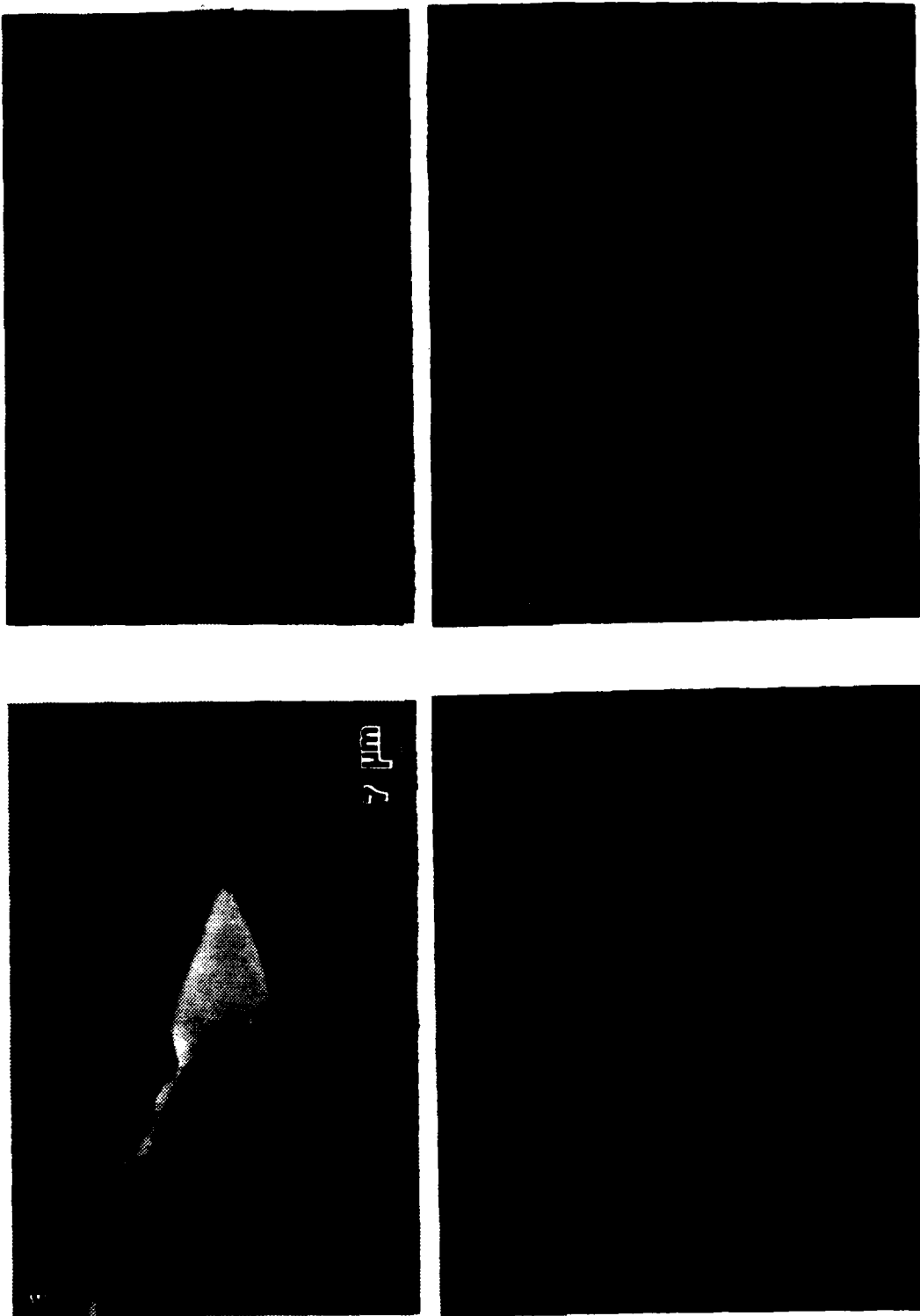


Figure 4.2 In (a) a $2rAl_3$ particle is shown in a deformed test specimen; (b) is an energy dispersive map of the particle; (c) shows the energy-dispersive X-Ray spectrum of the particle and (d) shows the energy-dispersive X-Ray spectrum of the surrounding matrix.

surrounding matrix. This shows the angular light-appearing particle to be Zr-rich, consistent with it being ZrAl_3 .

The phase diagram for the ternary Al-Mg-Zr system is not known in detail. From the binary diagram, Figure 4.3, 0.1%Zr should remain in the liquid until solidification occurs upon crossing the liquid and Al solid solution two phase region. The appearance and location of coarse β_{Zr} (ZrAl_3) suggests that this phase forms as a primary phase and serves further as nucleation sites for the Al solid solution. In the ternary Al-Mg-Zr system the peritectic reaction of Figure 4.3 likely would be connected to the eutectic in the Al-Mg binary (Figure 1.1). Since the Al-Mg eutectic temperature is much lower, 450°C, than the peritectic in the Al-Zr system, 660°C, it is likely that the minimum solubility of Zr in the liquid decreases from its value in the binary, 0.11%, to a lesser value. Mondolfo [Ref. 30] also suggests that there may be a ternary eutectic in the Al-Mg-Zr system near the Al-Mg binary eutectic, involving Al solid solution, β_{Zr} (ZrAl_3) and β_{Mg} (Mg_5Al_8). This latter would suggest that the grain boundaries of the as-cast material may comprise this ternary eutectic and hence contain additional β_{Zr} . This latter point was not pursued in this research.

2. Solution-Treated Microstructure

Solution treatment, i.e., heating for a period of time at a temperature at which a single-phase solid solution

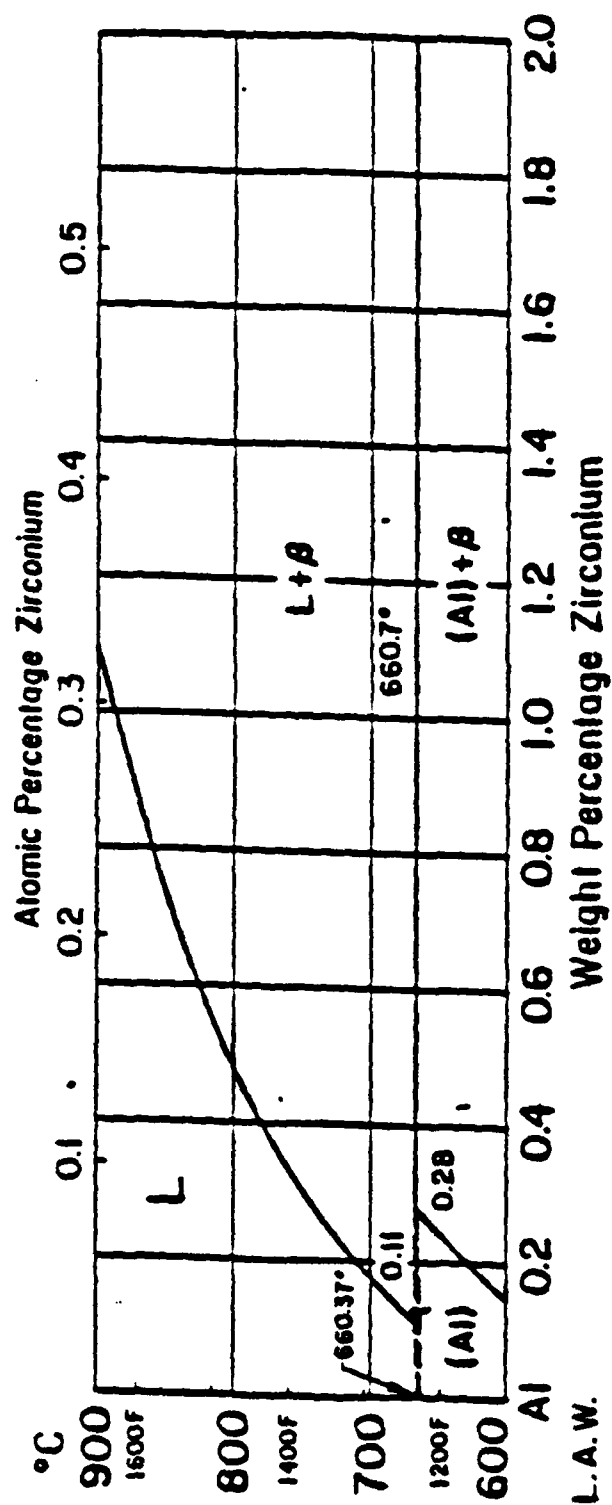


Figure 4.3 Partial aluminum-zirconium phase diagram

is stable, is the process by which microscopic differences in composition are reduced. For the high-magnesium alloy studied in this research, this requires heating in the single-phase region denoted α on the partial aluminum-magnesium phase diagram, Figure 1.1.

The temperature of solution treatment used in this research was selected for two reasons: first, burning must not occur and second, nearly complete resolution at reasonable times must occur. Since the beta (Mg_5Al_8) phase melts at $450^\circ C$, this temperature must not be exceeded. Since 10% magnesium is soluble in aluminum only above $360^\circ C$, the solution temperature must be above this. A temperature of $440^\circ C$ was selected as the highest practical temperature in this range, providing a reasonably short solution time. A solution treatment time of 24 hours was used as a result of Shirah's research [Ref. 8]. Shirah showed that after a 24 hour solution treatment time at $440^\circ C$ little if any improvement in homogeneity was made.

Figure 4.4 shows the solution treated microstructure of an Al-10%Mg-0.1%Zr alloy. Although solutioning of the beta precipitate (Mg_5Al_8) has taken place, the $ZrAl_3$ particles are still present in the center of the grains. Also, a considerable increase in grain size has occurred indicating that little, if any, grain boundary pinning has occurred.



Figure 4.4 Optical micrographs of an Al-10%Mg-0.1%Zr alloy solution treated 24 hours at 440°C and then oil quenched: (a) and (b) show $ZrAl_3$ particles (denoted by arrows) present as before; (c) and (d) are polarized light micrographs showing a much more homogeneous structure

3. Upset-Forged Microstructure

Upset forging, i.e., hotworking, is plastic deformation at a temperature in which a single phase is present. An isothermal forging was performed after the solution treatment to further refine and homogenize the cast microstructure.

In this study, an isothermal upset-forging at 440 °C was done after 24 hours of solution treatment. The billet was then annealed for one hour at the solution treatment temperature prior to oil quenching to insure a quenching temperature from above the solvus.

Figure 4.5 shows the microstructure of a solution treated, upset-forged, annealed (1 hour at 440 °C) and oil quenched Al-10%Mg-0.1%Zr alloy. It has become even more homogeneous in appearance, however, as before the $ZrAl_3$ particles are still present. Additionally, it appears that recrystallization has occurred since grain size is now smaller than before.

4. Warm-Rolled Microstructure

Rolling consists of passing a work piece of a deformable material between parallel, rotating steel cylinders of separation less than the thickness of the piece. This reduction in thickness results in plastic deformation. The warm working range of a high-magnesium alloy is considered to be temperatures between 200 °C and the



Figure 4.5 Optical micrographs of an Al-10%Mg-0.1%Zr alloy solution treated 24 hours at 440°C, up-set forged, annealed 1 hour at 440°C and oil quenched: (a) and (b) show $ZrAl_3$ particles (denoted by arrows) present as before and (c) and (d) are polarized light micrographs showing an even more homogeneous structure.

solvus. Here, a rolling temperature of 300°C was employed as a result of Grandon's work [Ref. 4].

Utilizing the same rolling procedure employed in this research, McNelley and Garg [Ref. 31] found in an Al-10.2%Mg alloy that precipitation of intermetallic beta (Mg_5Al_8) occurred at rolling strains between 0.6 and 1.0. Thereafter, for increased true rolling strain the content of magnesium in solid solution leveled off at 7.2%, a reflection of the approximate solubility limit of magnesium in aluminum at this temperature. Figure 4.6 illustrates the precipitation of magnesium during warm rolling and the corresponding increase in ambient temperature hardness with the increase of true rolling strain [Ref. 30].

Figure 4.7 consists of tri-planar micrographs of the Al-10%Mg-0.1%Zr alloy rolled to three different strains. An obvious increase in beta precipitate is noted between micrographs (a) and (b), whereas little, if any, increase in beta precipitate is noted between micrographs (b) and (c). With reference to McNelley's and Garg's work previously described, this is probably due to the solubility limit of magnesium in aluminum at this temperature. From the transmission electron microscopy conducted on the as-rolled material, it is evident that the beta precipitate (Mg_5Al_8) is much smaller than it appears in the optical micrographs. Hence, it is believed that the etchant overemphasizes the

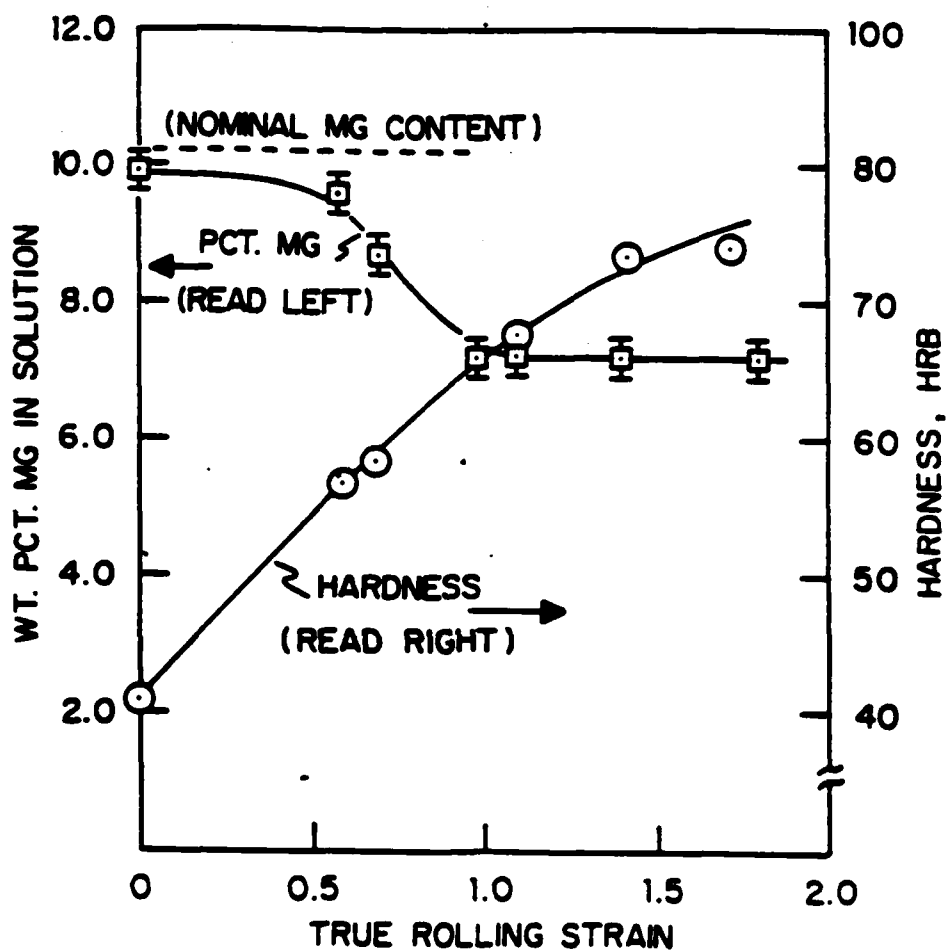


Figure 4.6 The increase in hardness and the precipitation of Mg from solution during warm rolling. Data from McNelley and Garg [Ref. 31].

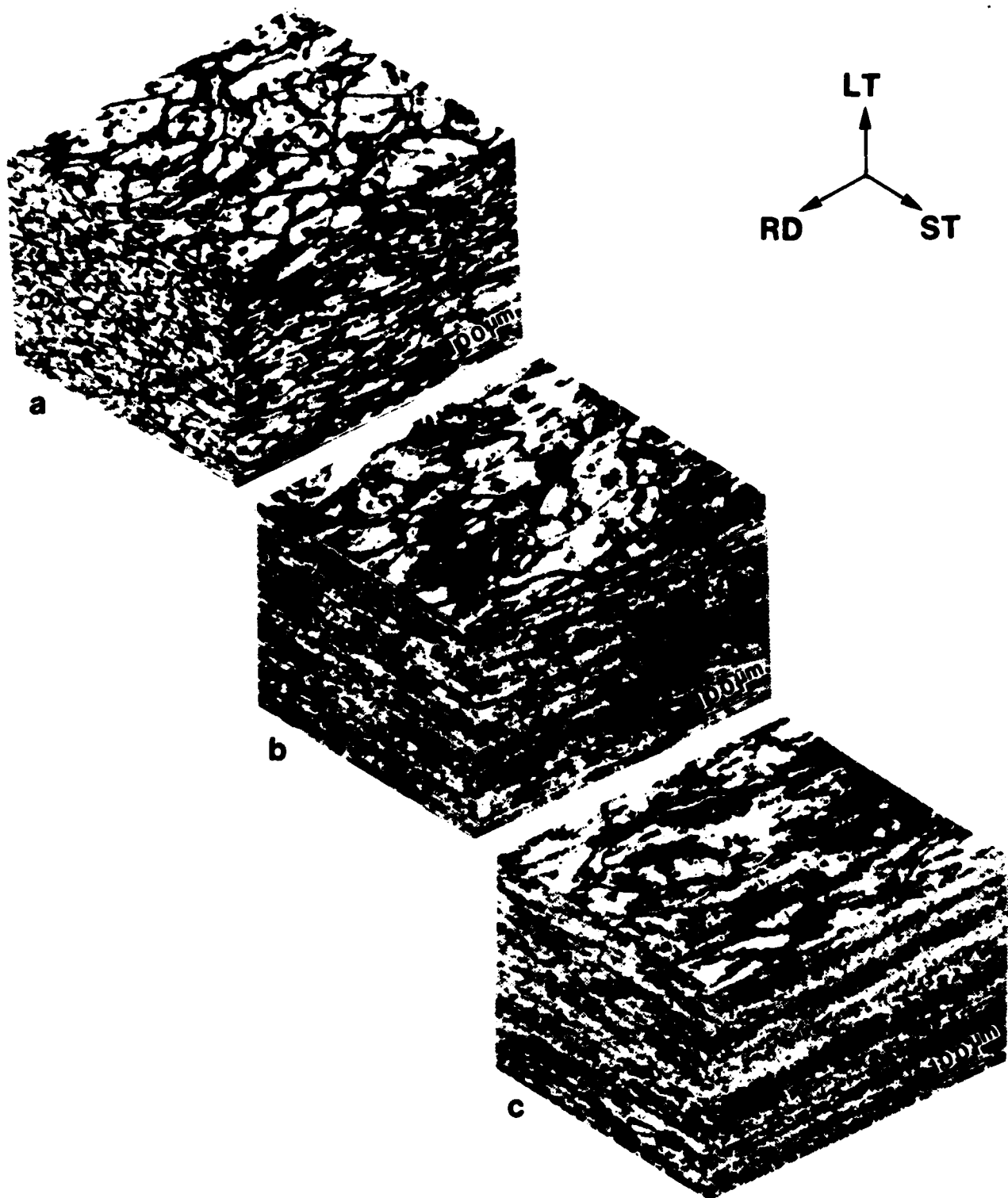


Figure 4.7 Tri-planar micrographs of an Al-10%Mg-0.1%Zr alloy warm rolled at 300°C to three different strains: (a) $e \approx .55$, (b) $e \approx .77$ and (c) $e \approx .91$.

Hence, it is believed that the etchant overemphasizes the precipitation occurring in the alloy. It is notable that precipitation became more uniformly distributed with increasing strain, reflecting a break-up and refinement during deformation.

Figure 4.8 shows the high dislocation density resulting from warm rolling at 300°C to a true strain of 2.3. The substructure is disorganized, with limited recovery having occurred.

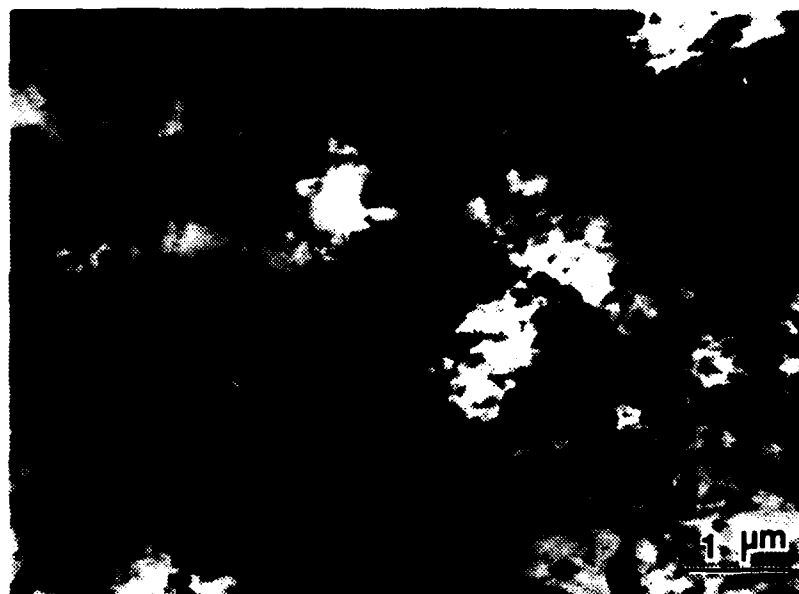


Figure 4.8 TEM micrograph of an Al-10%Mg-0.1%Zr alloy warm rolled at 300°C and air cooled to room temperature.

B. MICROSTRUCTURAL EXAMINATION OF AS-ROLLED TEST SPECIMENS

1. Specimens Tested at 200 °C

Specimens tested at a temperature of 200 °C and strain rates of $6.67 \times 10^{-2} \text{s}^{-1}$, $6.67 \times 10^{-3} \text{s}^{-1}$ and $6.67 \times 10^{-4} \text{s}^{-1}$ were optically examined. Figure 4.9 illustrates that none of these test specimens reached superplastic elongations.

Optical micrographs, Figures 4.10, 4.11, and 4.12, reveal that as strain rate is increased, the grain shape becomes more elongated. This grain elongation reflects dislocation mechanisms controlling plastic deformation at this temperature. The specimen having the more equiaxed grain structure has better elongations. Two other features of these microstructures that are important to note are: (1) the homogeneity of the structure has improved over the as-rolled condition and (2) no cavitation (coalescence of microvoids) has occurred. At this low test temperature, diffusion, which is a thermally activated process, is suppressed, resulting in minimal boundary sliding, decohesion, and cavitation.

Figure 4.13 shows the very fine substructure of two 200 °C test specimens, one deformed at a strain rate of $6.67 \times 10^{-3} \text{s}^{-1}$, and the other deformed at a strain rate of $6.67 \times 10^{-4} \text{s}^{-1}$. Both reveal a subgrain structure of similar subgrain size; these structures appear recovered relative to the as-rolled condition (Figure 4.8) but the structure is still somewhat diffuse.

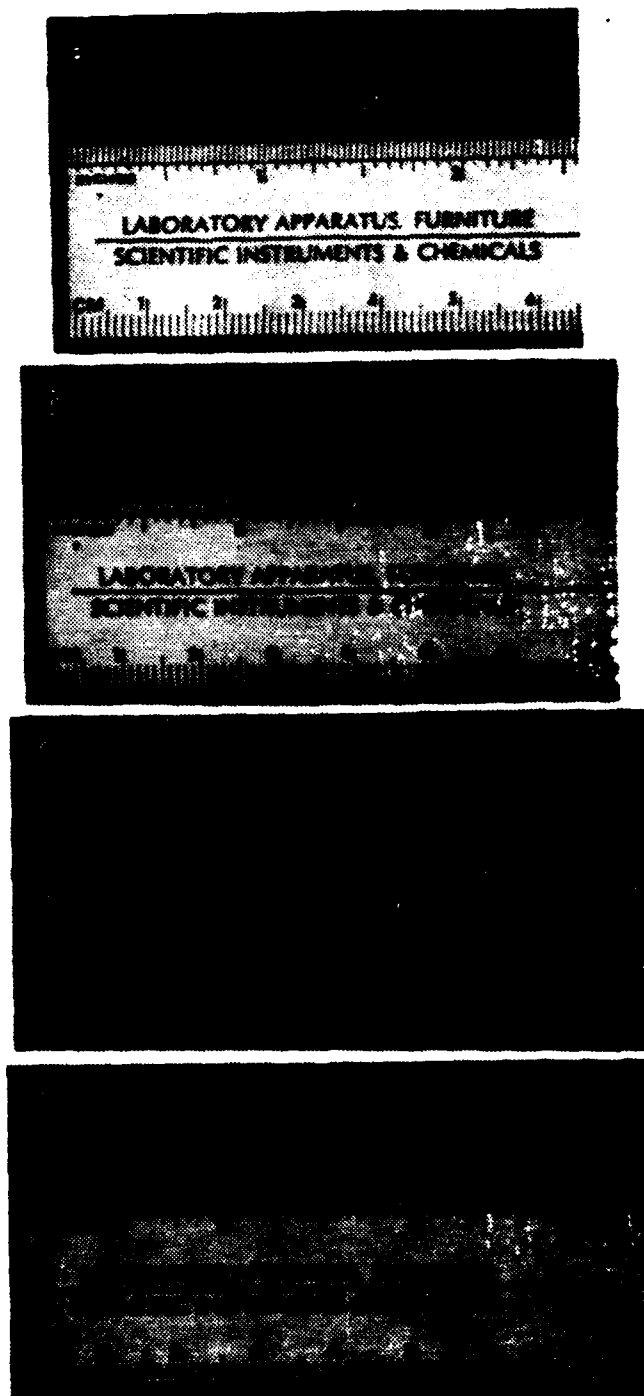


Figure 4.9 Photographs of 200°C test specimens: (a) untested, (b) deformed to fracture at $\dot{\epsilon} = 6.67 \times 10^{-2} \text{ s}^{-1}$, elongation 70%, (c) deformed to fracture at $\dot{\epsilon} = 6.67 \times 10^{-3} \text{ s}^{-1}$, elongation 107%, and (d) deformed to fracture at $\dot{\epsilon} = 6.67 \times 10^{-4} \text{ s}^{-1}$, elongation 127%.

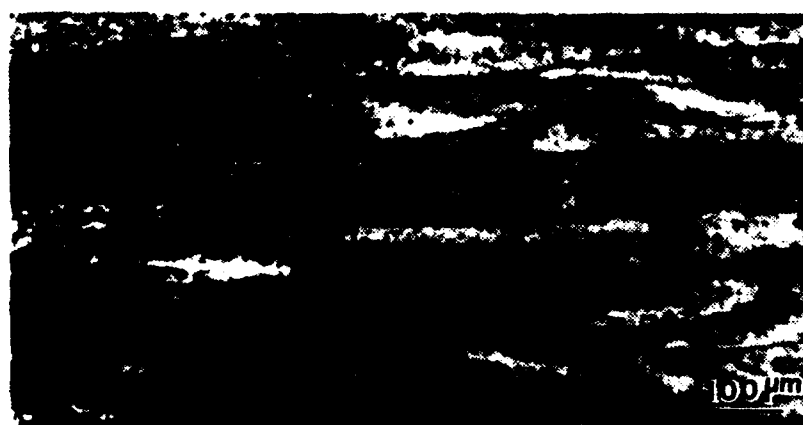


Figure 4.10 Optical micrographs of a test specimen deformed to fracture at 100°C and $\dot{\epsilon} = 6.67 \times 10^{-2} \text{ s}^{-1}$; (a) fracture point, (b) gage section and (c) grip section.

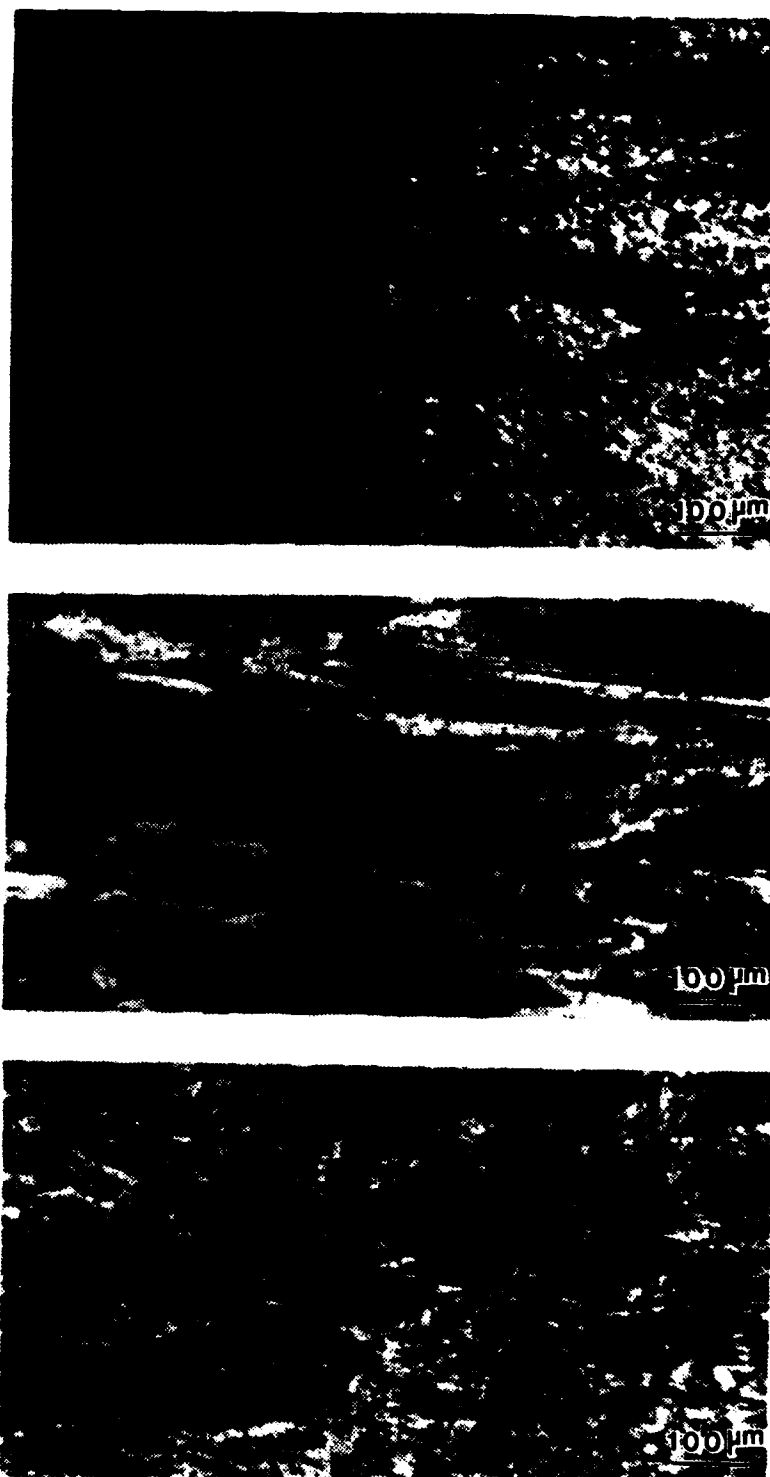


Figure 4.11 Optical micrographs of a test specimen deformed to fracture at 100°C and $\dot{\epsilon} = 6.67 \times 10^{-3} \text{ s}^{-1}$: (a) fracture point, (b) gage section and (c) grip section.

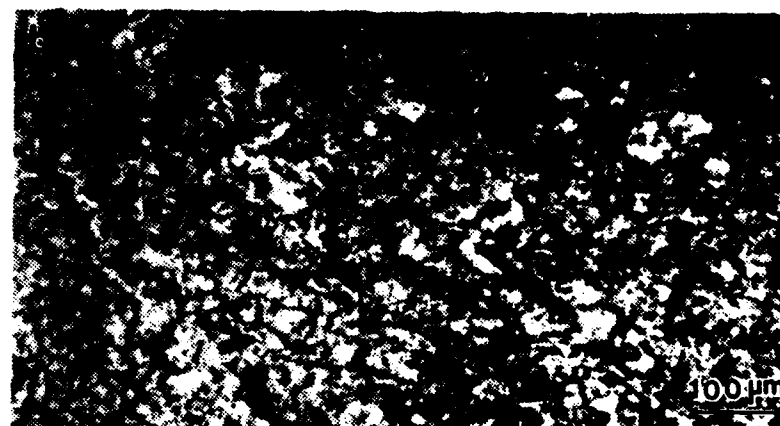


Figure 4.12 Optical micrographs of a test specimen deformed to fracture at 100 °C and $\dot{\epsilon} = 6.67 \times 10^{-4} \text{ s}^{-1}$: (a) fracture point, (b) gage section and (c) grip section.

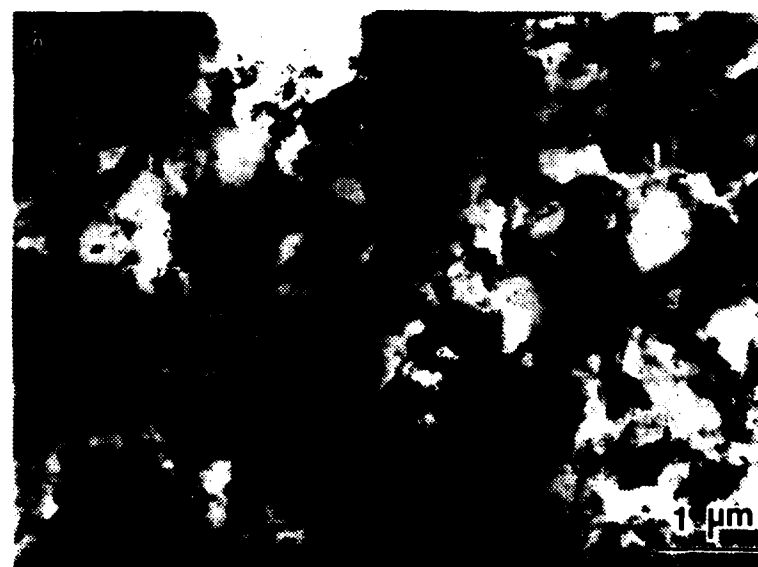
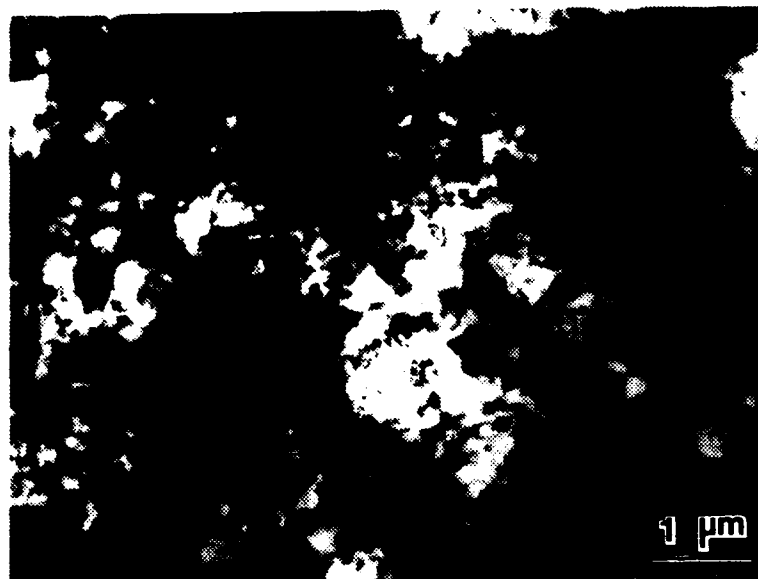


Figure 4.13 TEM micrographs of 200 °C test specimen:
 (a) deformed to fracture at $\dot{\epsilon} = 6.67 \times 10^{-3} \text{ s}^{-1}$ and
 (b) deformed to fracture at $\dot{\epsilon} = 6.67 \times 10^{-4} \text{ s}^{-1}$.

2. Specimens Tested at 300 °C

Specimens tested at 300 °C and strain rates of $6.67 \times 10^{-2} \text{ s}^{-1}$, $6.67 \times 10^{-3} \text{ s}^{-1}$, and $6.67 \times 10^{-4} \text{ s}^{-1}$ were also examined. All exhibited superplastic elongations. Figure 4.14 illustrates the effect that strain rate has on superplasticity at this test temperature. Tensile testing at an intermediate strain rate of $6.67 \times 10^{-3} \text{ s}^{-1}$ results in better superplastic elongations than those tested at $6.67 \times 10^{-2} \text{ s}^{-1}$ and $6.67 \times 10^{-4} \text{ s}^{-1}$.

Figures 4.15, 4.16, and 4.17 are optical micrographs of each test specimen examined. Like the 200 °C test specimens, an elongated grain structure is evident in the least ductile of these specimens. In the deformed sections of the test specimens tested at $6.67 \times 10^{-3} \text{ s}^{-1}$ and $6.67 \times 10^{-4} \text{ s}^{-1}$ no grain structure is even evident optically. Rather, a very homogeneous precipitated structure is revealed. Unlike the 200 °C test specimens, these test specimens have some cavitation present. The minor cavitation that is present is located near the fracture point and is in the form of stringers. This cavitation is attributed to the presence of the ZrAl_3 particles.

Transmission electron micrographs, Figure 4.18, show a microstructure consisting of both high and low angle grain boundaries. The test specimen exposed to the faster strain rate has the smaller grain and subgrain size. This is

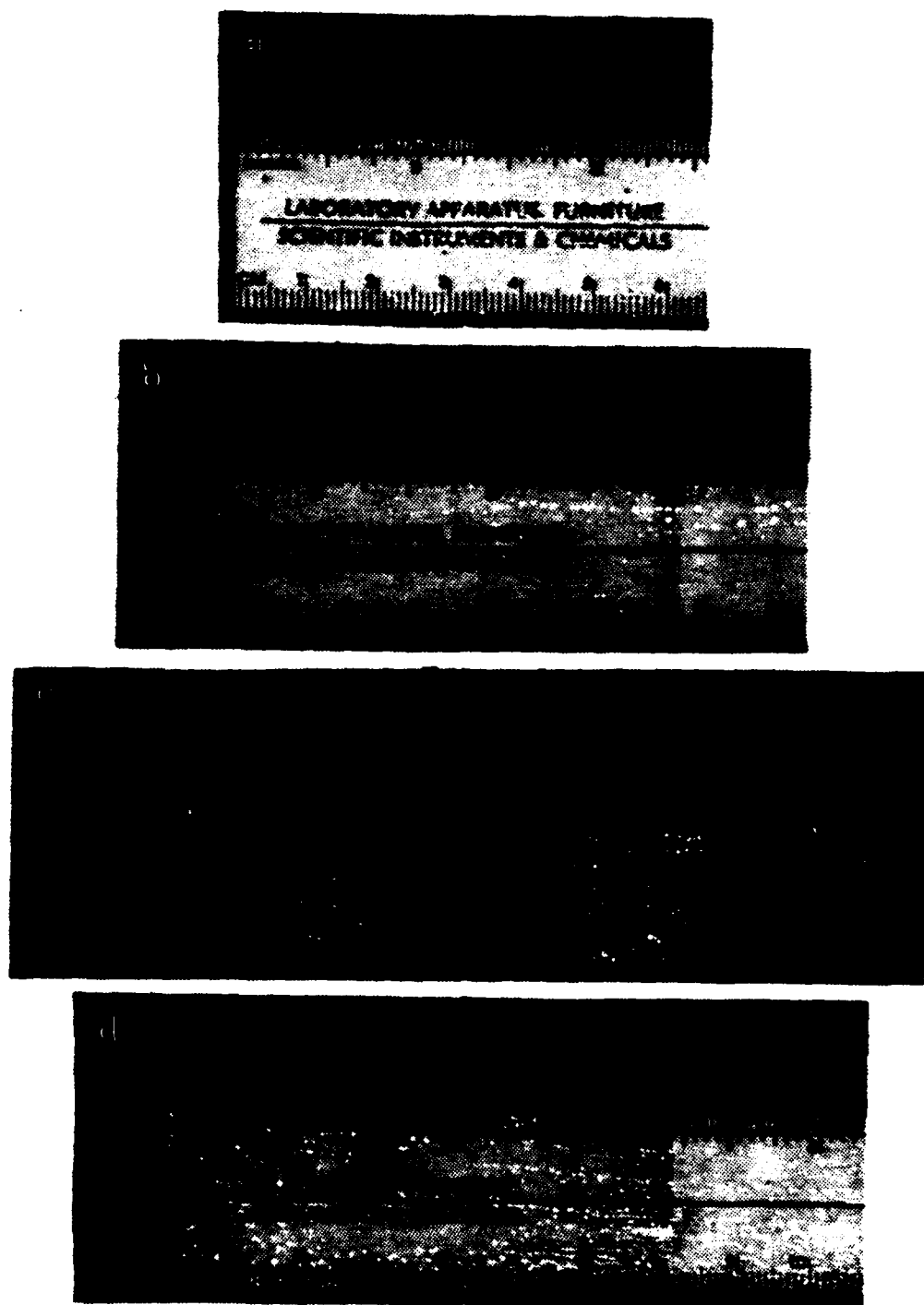


Figure 4.14 Photographs of 300°C test specimens: (a) untested, (b) deformed to fracture at $\dot{\epsilon} = 6.67 \times 10^{-2} \text{ s}^{-1}$, elongation 221%, (c) deformed to fracture at $\dot{\epsilon} = 6.67 \times 10^{-3} \text{ s}^{-1}$, elongation 480%, and (d) deformed to fracture at $\dot{\epsilon} = 6.67 \times 10^{-4} \text{ s}^{-1}$, elongation 330%.

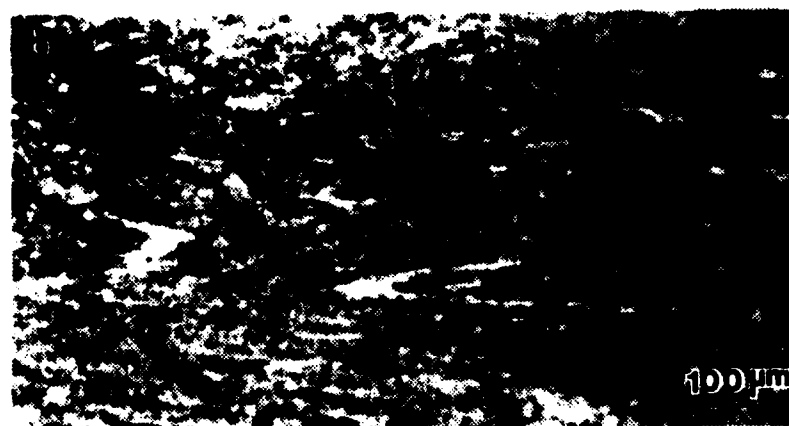
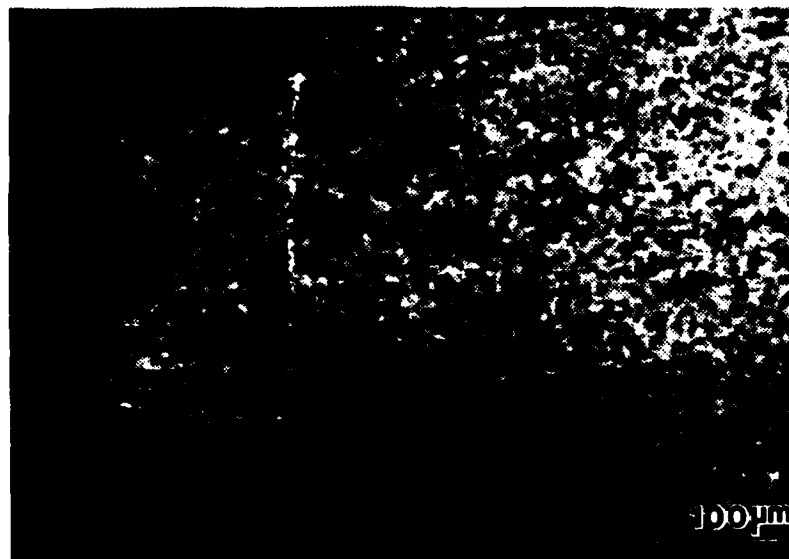


Figure 4.15 Optical micrographs of a test specimen deformed to fracture at 300°C and $\dot{\epsilon} = 6.67 \times 10^{-2} \text{ s}^{-1}$: (a) fracture point, (b) gage section and (c) grip section.

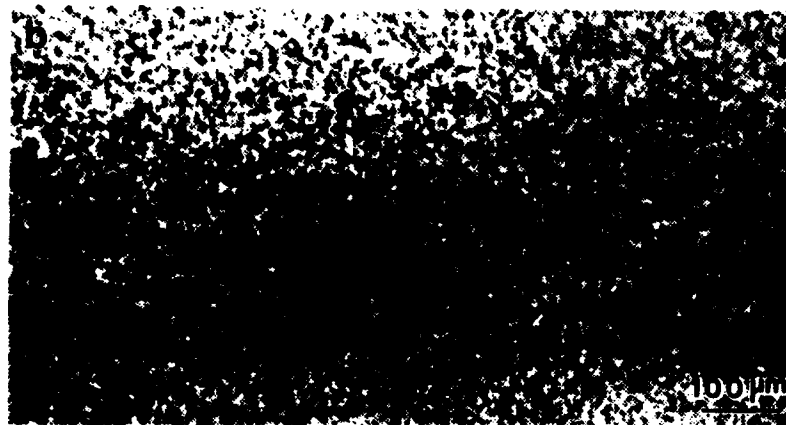
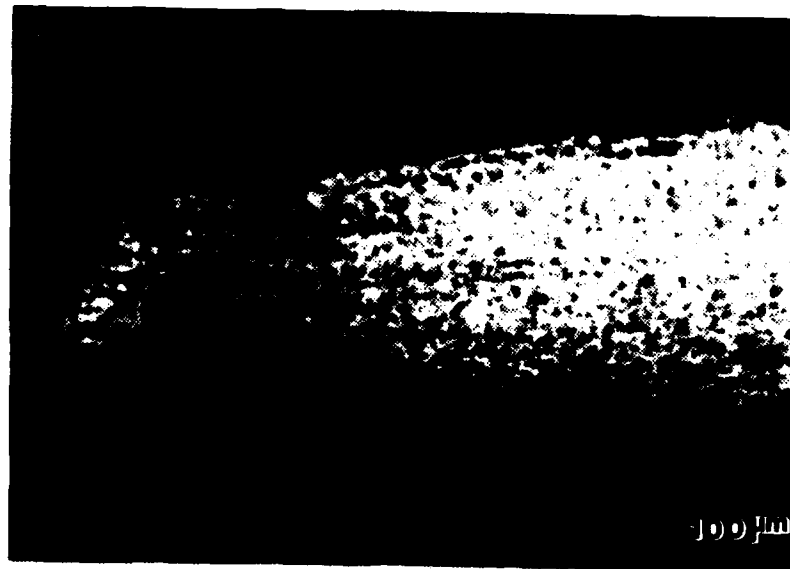


Figure 4.16 Optical micrographs of a test specimen deformed to fracture at 300°C and $\dot{\epsilon} = 6.67 \times 10^{-3} \text{ s}^{-1}$: (a) fracture point, (b) gage section and (c) grip section.

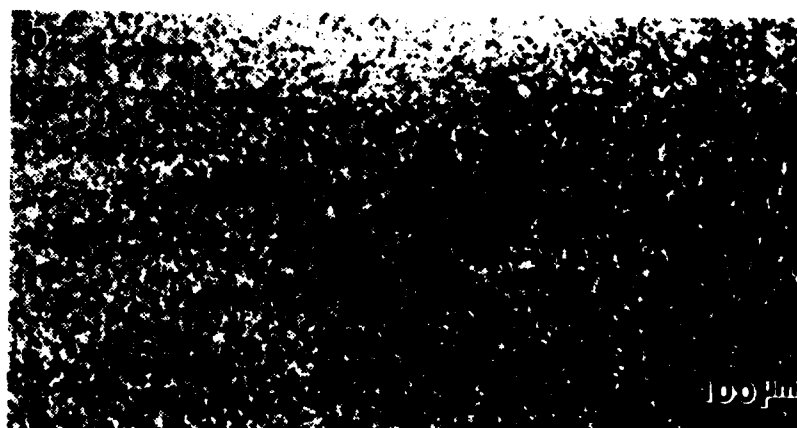
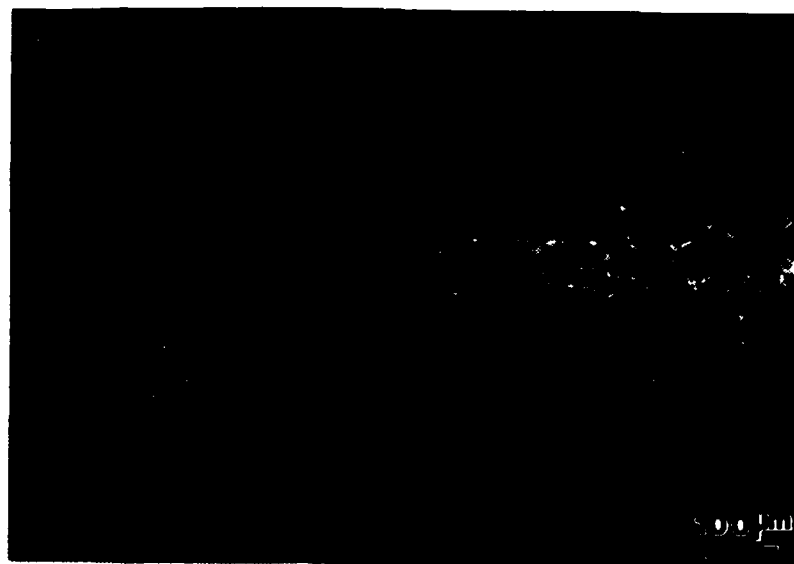


Figure 4.17 Optical micrographs of a test specimen deformed to fracture at 300°C and $\dot{\epsilon} = 6.67 \times 10^{-4} \text{s}^{-1}$: (a) fracture point, (b) gage section and (c) grip section.



Figure 4.18 TEM micrographs of 300 °C test specimen:
 (a) deformed to fracture at $\dot{\epsilon} = 6.67 \times 10^{-3} \text{ s}^{-1}$ and
 (b) deformed to fracture at $\dot{\epsilon} = 6.67 \times 10^{-4} \text{ s}^{-1}$.

attributed to the higher rates imposed during testing and the resultant higher flow stress with reduced time at temperature as well. This results in more low angle grain boundaries. Comparing this substructure to the substructure of the 200°C test specimens (Figure 4.13), it is evident that this structure is much more completely recovered and clearly defined.

The initial microstructure of this alloy contradicts the current theories discussed in the background of this thesis, which predict superplasticity only in alloys with fine, high angle, recrystallized grains. Here, a method by which high-magnesium aluminum magnesium alloys can be processed for superplastic deformation at warm temperatures, with negligible cavitation, has been developed. This regime of superplastic deformation relies upon recovery and possibly continuous recrystallization during deformation at relative low temperatures. Although this method is illustrated in this thesis work, it is the product of many years of research at the Naval Postgraduate School.

3. Specimens Tested at 400°C

Figure 4.19 shows photographs of test specimens tested at 400°C and strain rates of $6.67 \times 10^{-2} \text{s}^{-1}$, $6.67 \times 10^{-3} \text{s}^{-1}$, and $6.67 \times 10^{-4} \text{s}^{-1}$. Superplastic elongation was only noted in the test specimens tested at the two slower strain rates; furthermore, the elongations attained are below those of corresponding strain rates tested at 300°C.

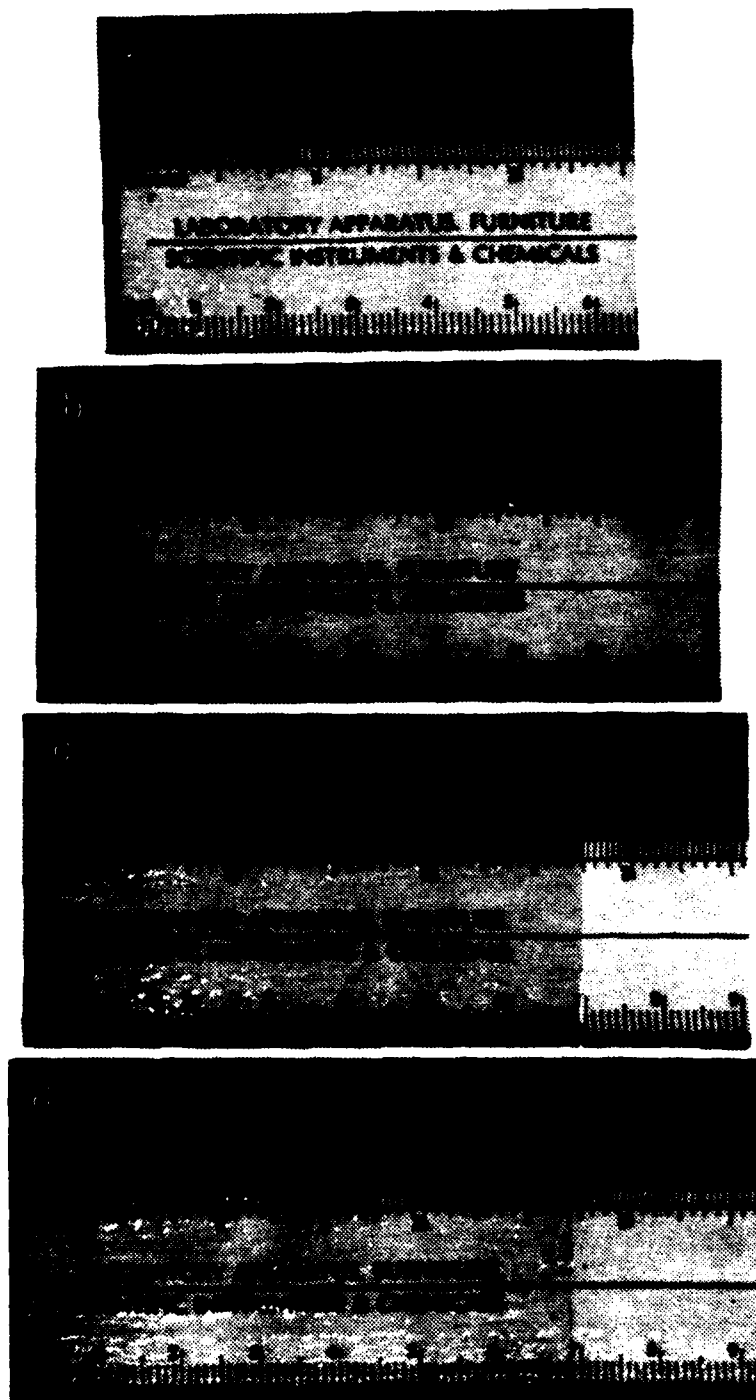


Figure 4.19 Photographs of 400 °C test specimens: (a) untested, (b) deformed to fracture at $\dot{\epsilon} = 6.67 \times 10^{-2} \text{s}^{-1}$, elongation 168%, (c) deformed to fracture at $\dot{\epsilon} = 6.67 \times 10^{-3} \text{s}^{-1}$, elongation 204%, and (d) deformed to fracture at $\dot{\epsilon} = 6.67 \times 10^{-4} \text{s}^{-1}$, elongation 222%.

Micrographs obtained for these test specimens, Figures 4.20, 4.21, and 4.22, reveal that recrystallization has occurred. This was expected, since the test temperature is above the solvus. In comparing the grain structure near the fracture point with that of the intermediate gage section and also the grip section, it can be seen that the microstructure of these test specimens is unstable at this test temperature, resulting in banding and extensive grain growth. This instability may be a result of the material having non-uniform zirconium distribution. These specimens show cavitation, which would lead to service property degradation. Unlike the large, equiaxed cavities that result from grain boundary sliding, these cavities appear in the form of stringers, cutting across grains. As shown in Figure 4.23 the ZrAl_3 particles act as initiation sites for these long stringers of cavities. The plastic deformation of the surrounding matrix results in their subsequent growth. Contrary to results typically observed [Ref. 15], cavitation is more extensive at the higher strain rate. This is attributed to the grain growth, especially prevalent at lower strain rates. The presence of substantial grain boundary migration may tend to relieve the localized stress concentrations that are considered a prerequisite for cavity formation.

Figure 4.24 shows transmission electron micrographs of two 400 °C test specimens. One was tested at a strain

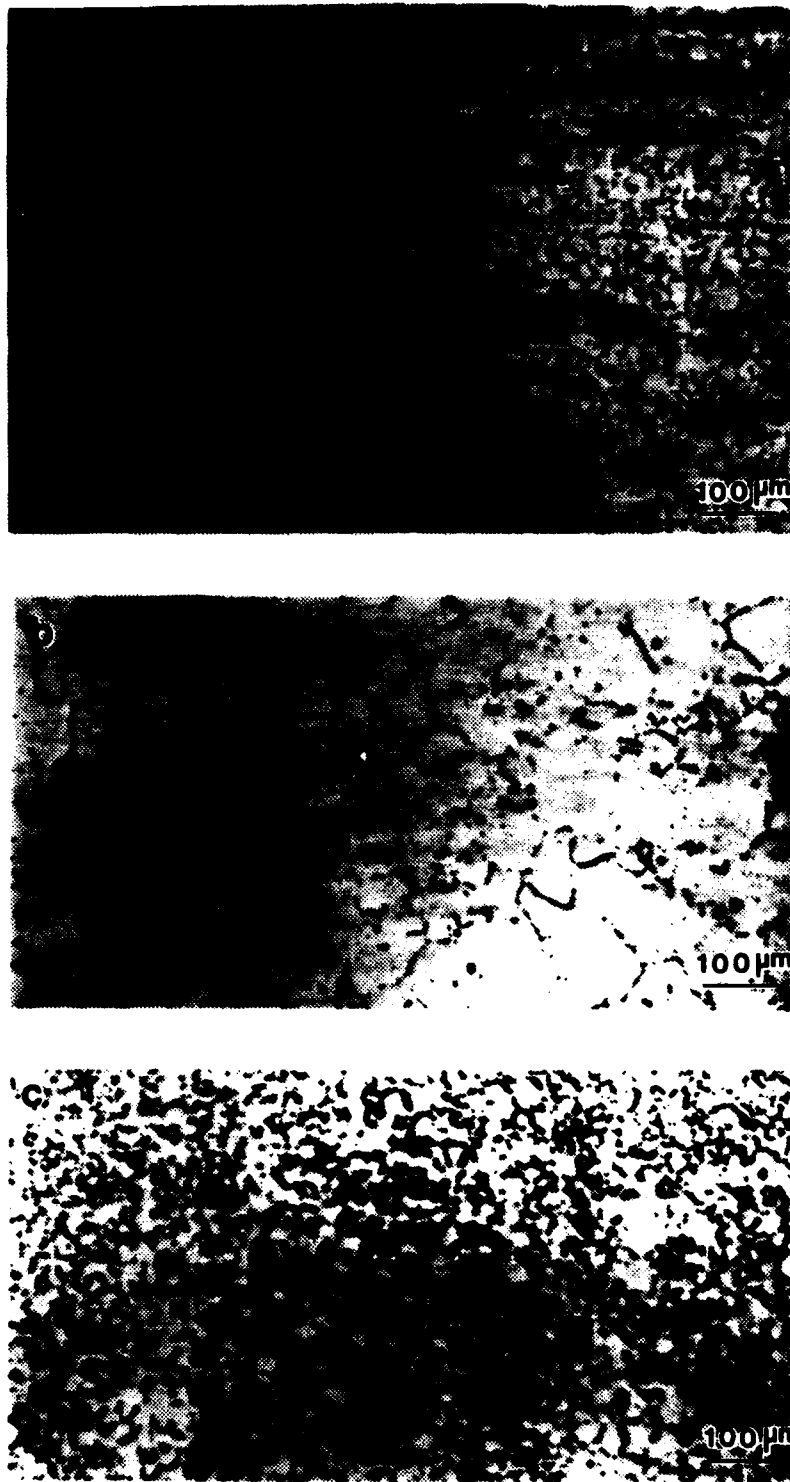


Figure 4.20 Optical micrographs of a test specimen deformed to fracture at 400°C and $\dot{\epsilon} = 6.67 \times 10^{-2} \text{ s}^{-1}$; (a) fracture point, (b) gage section and (c) grip section.

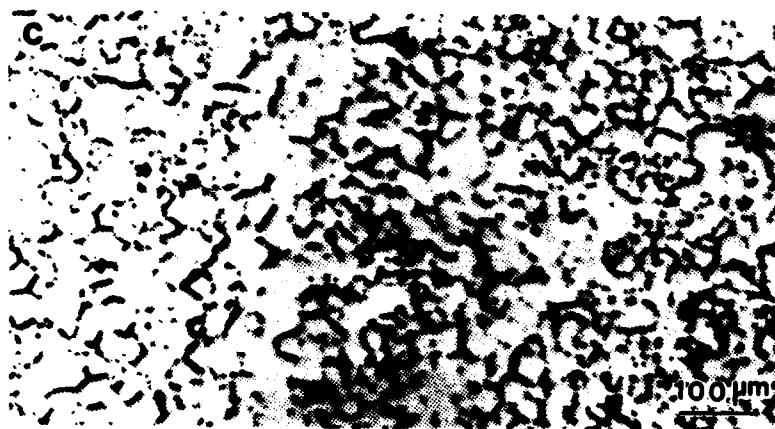
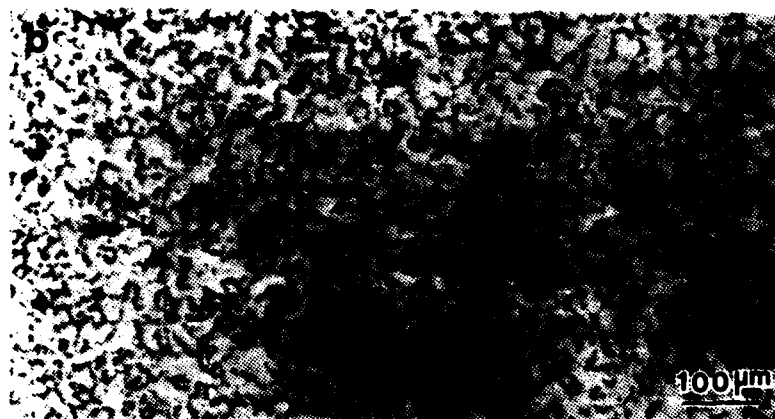
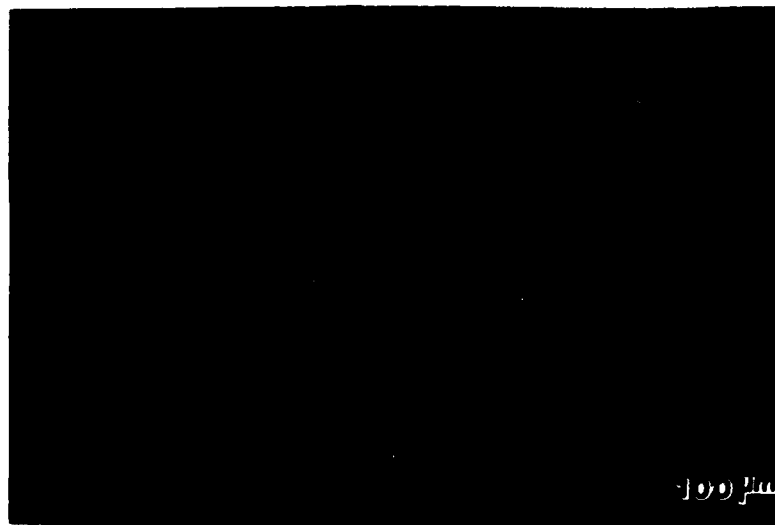


Figure 4.21 Optical micrographs of a test specimen deformed to fracture at 400 °C and $\dot{\epsilon} = 6.67 \times 10^{-3} \text{ s}^{-1}$: (a) fracture point, (b) gage section and (c) grip section.

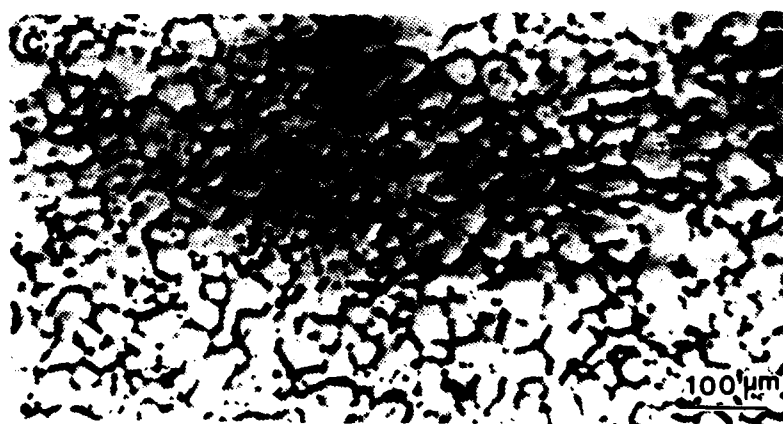
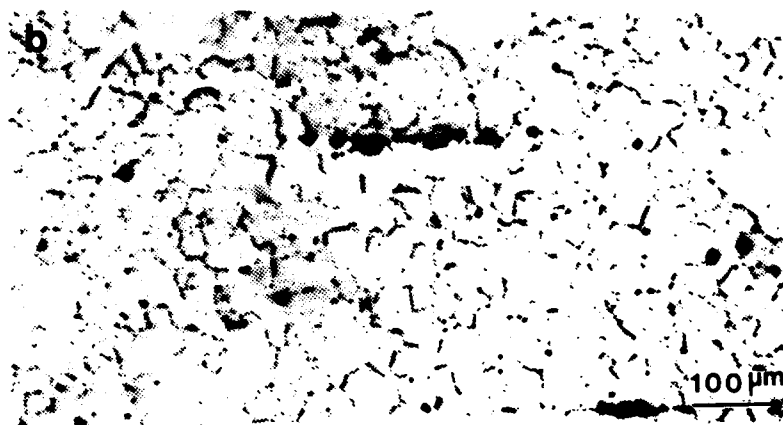
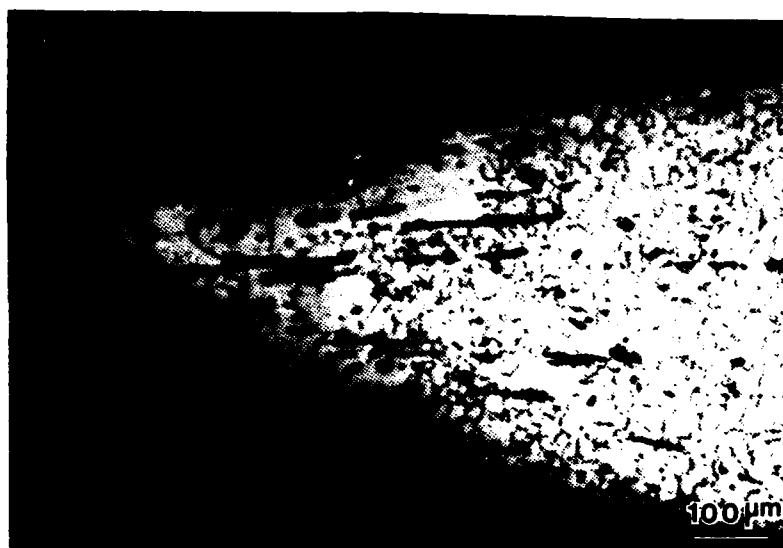


Figure 4.22 Optical micrographs of a test specimen deformed to fracture at 400°C and $\dot{\epsilon} = 6.67 \times 10^{-4} \text{s}^{-1}$: (a) fracture point, (b) gage section and (c) grip section.

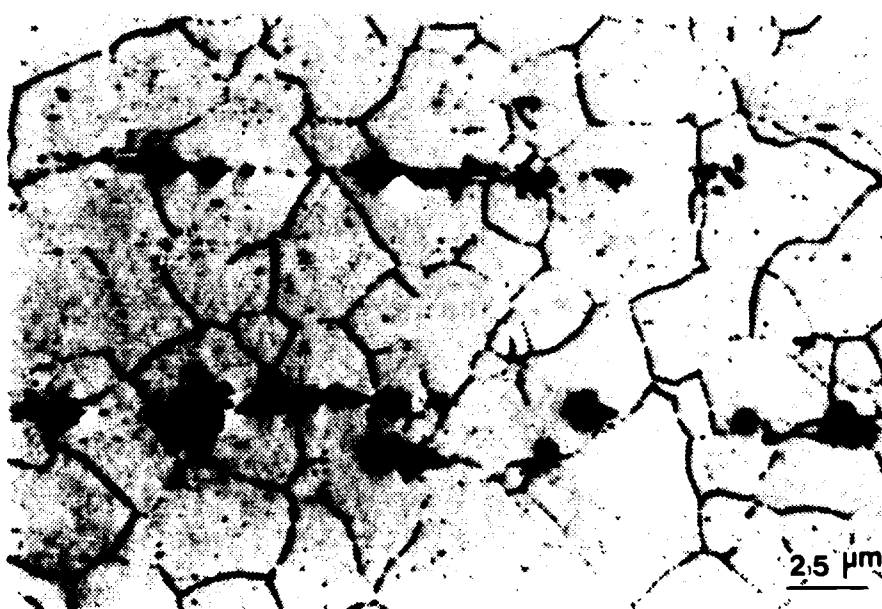
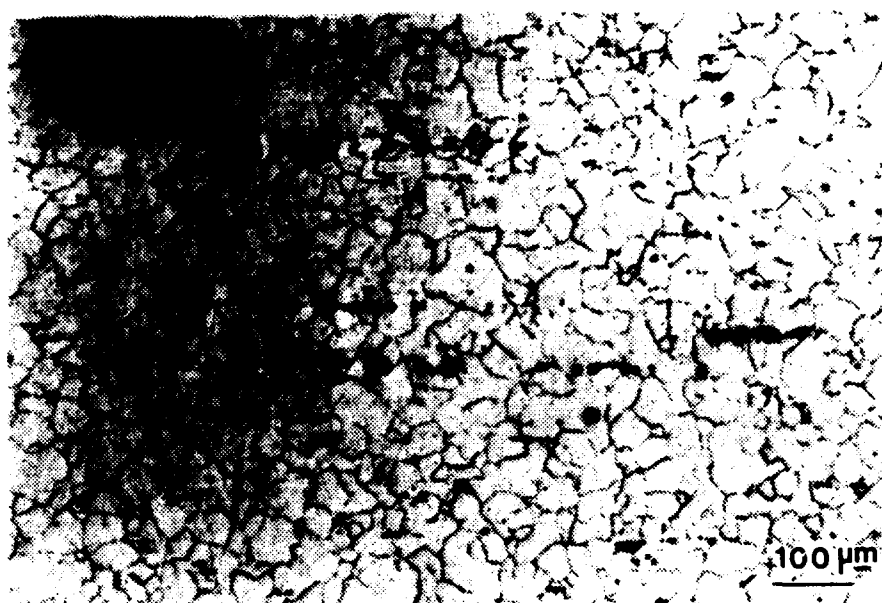


Figure 4.23 Optical micrographs showing $ZrAl_3$ particles present within cavity stringers in a test specimen deformed at 400 °C.

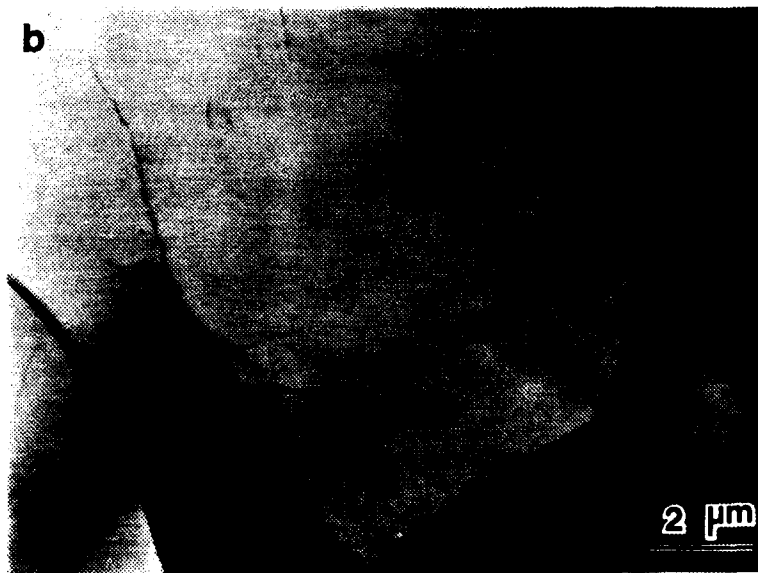
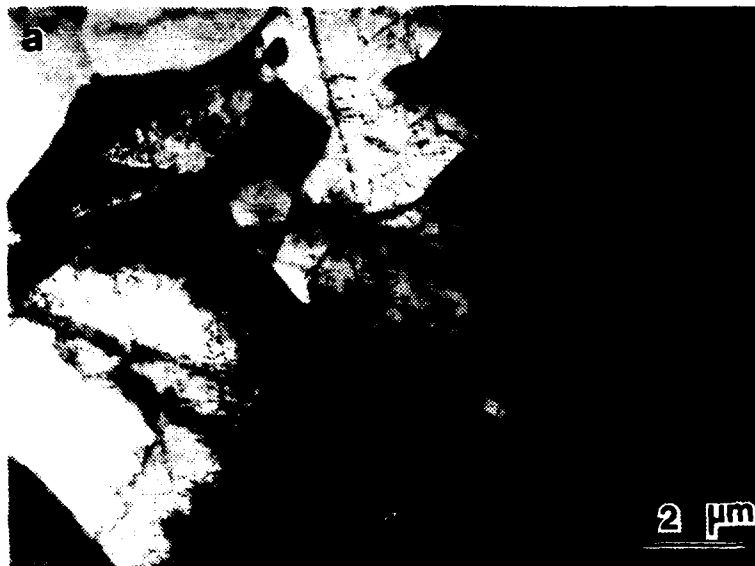


Figure 4.24 TEM micrographs of 400 °C test specimen:
 (a) deformed to fracture at $\dot{\epsilon} = 6.67 \times 10^{-3} \text{ s}^{-1}$ and
 (b) deformed to fracture at $\dot{\epsilon} = 6.67 \times 10^{-4} \text{ s}^{-1}$.

rate of $6.67 \times 10^{-3} \text{s}^{-1}$ and the other was tested at a strain rate of $6.67 \times 10^{-4} \text{s}^{-1}$. Evident in these micrographs is large grain size and high angle grain boundaries. Also, the formation of low angle subgrains appears to be taking place. The specimen deformed at the faster strain rate has a higher dislocation density and thus a finer subgrain structure developing. Figure 4.25 shows the dislocations rearranging themselves into a subgrain configuration. Also revealed are dislocation slip bands penetrating sub-boundaries, thus confirming these as low angle boundaries.

Figure 4.26 is a plot of test data obtained by Hartmann [Ref. 29] showing the effect that temperature has on flow stress. Recrystallization of the test specimens upon heating to the test temperature and prior to commencing a stress strain test is proposed to explain the increase in stress at a temperature approximately equal to the solvus ($\approx 350^\circ\text{C}$). It is assumed that this recrystallization took place before actual tensile testing, while waiting for isothermal conditions to be attained. This material readily recrystallizes at high temperatures (discussed in the next section), confirming this assumption. These observations emphasize that in actuality, test specimens tested at a temperature above the solvus were of a recrystallized microstructure as opposed to a rolled and recovered microstructure.

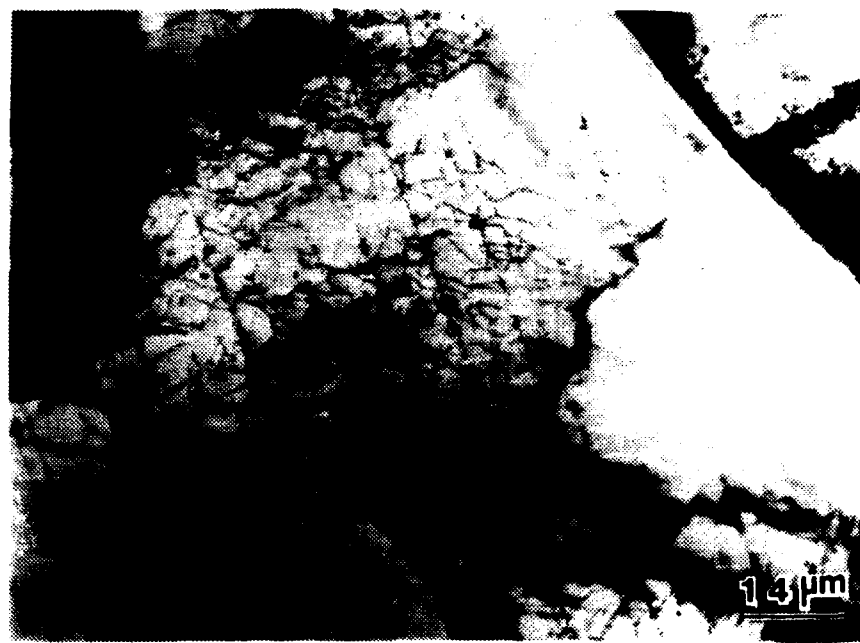


Figure 4.25 TEM micrographs showing dislocation arrangement into a subgrain configuration.

TRUE STRESS-VS-TEMPERATURE

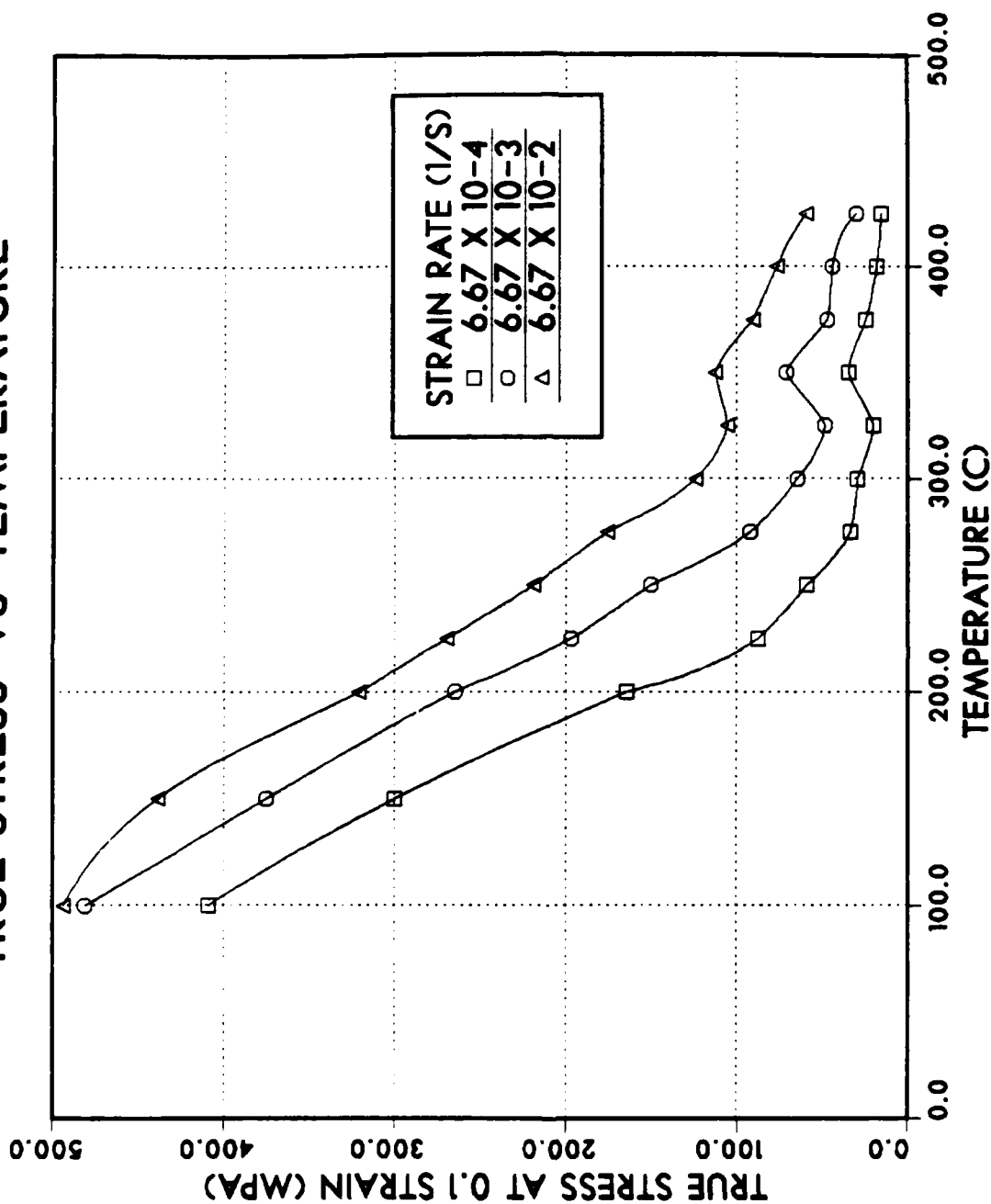


Figure 4.26 True stress at 0.1 strain vs. temperature for test specimens in the as-rolled condition.

C. MICROSTRUCTURAL EXAMINATION OF RECRYSTALLIZED TEST SPECIMENS

1. Recrystallization Treatment

At sufficiently high temperatures, a deformed metal will give up stored energy as minute new crystals make their appearance in the microstructure. These crystals appear first in the most severely distorted regions of the structure, usually at former grain boundaries or large constituent particles. The formation of these strain-free grains is one of nucleation and diffusion controlled growth and thus will only occur at elevated temperatures.

The primary reason for tensile testing recrystallized specimens was to obtain a comparison between the superplastic characteristics of the recrystallized and as-rolled test specimens. A time at which the structure would completely recrystallize when annealed at 440°C was sought. Figure 4.27 shows the effect that various times of annealing at 440°C has on the microstructure. As revealed here, this structure recrystallizes very fast at this temperature. This is attributed to the high strain energy introduced in the structure during warm rolling.

As a result of the microstructural data of Figure 4.27, tensile test specimens were annealed at 440°C for 60 seconds to attain recrystallization. Figure 4.28 shows the microstructure by TEM of an untested, recrystallized test specimen. As expected, this microstructure is essentially

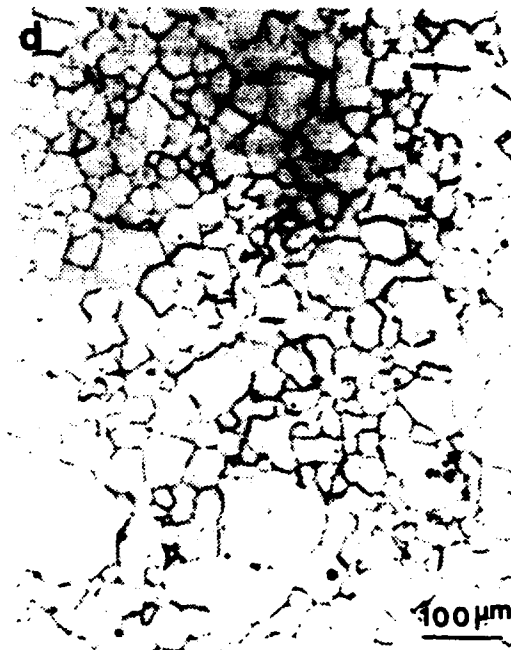
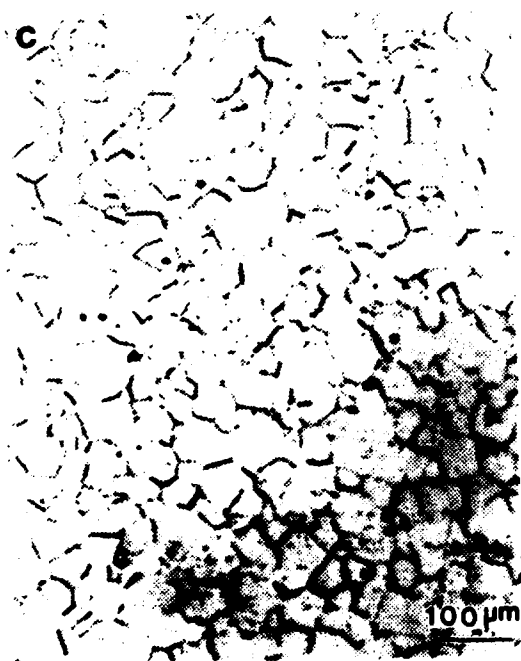


Figure 4.27 Optical micrographs of specimens annealed at 440 °C for (a) 30 sec; (b) 60 sec; (c) 5 minutes and (d) 30 minutes.

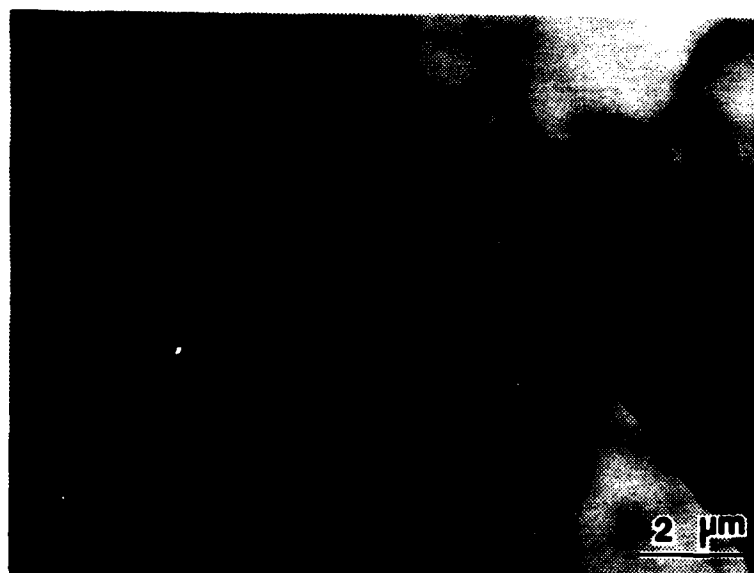


Figure 4.28 TEM micrograph of a recrystallized test specimen before deformation.

dislocation free with only high-angle boundary grains present. Evident in these micrographs is grain boundary interaction with dispersed particles.

2. Specimens Tested at 300 °C

Optical microscopy was conducted on tensile specimens first recrystallized and then tested at 300 °C and strain rates of $6.67 \times 10^{-2} \text{s}^{-1}$, $6.67 \times 10^{-3} \text{s}^{-1}$, and $6.67 \times 10^{-4} \text{s}^{-1}$. Figures 4.29, 4.30, and 4.31 show the microstructure of each specimen. These specimens did not show superplastic elongations during deformation and considerable cavitation did take place. These cavities are equiaxed in shape and appear to be the result of grain boundary sliding. Stress-assisted vacancy diffusion is considered the principle mechanism of this type cavitation.

3. Specimens Tested at 400 °C

These specimens, like the as-rolled specimens tested at this temperature, demonstrated superplastic elongations during deformation. As expected, Figure 4.32, 4.33, and 4.34 reveal that these specimens have the same basic microstructural characteristics as the as-rolled specimens tested at 400 °C. The only noticeable difference is grain size and amount of cavitation present. The microstructures of these specimens show a larger grain size and a smaller amount of cavitation than those of the as-rolled material tested at 400 °C. As discussed in the previous section, the difference in amount of cavitation is attributed to the



Figure 4.29 Optical micrographs of a recrystallized test specimen deformed at 300°C and $\dot{\epsilon} = 6.67 \times 10^{-2} \text{s}^{-1}$: (a) fracture point, (b) gage section and (c) grip section.

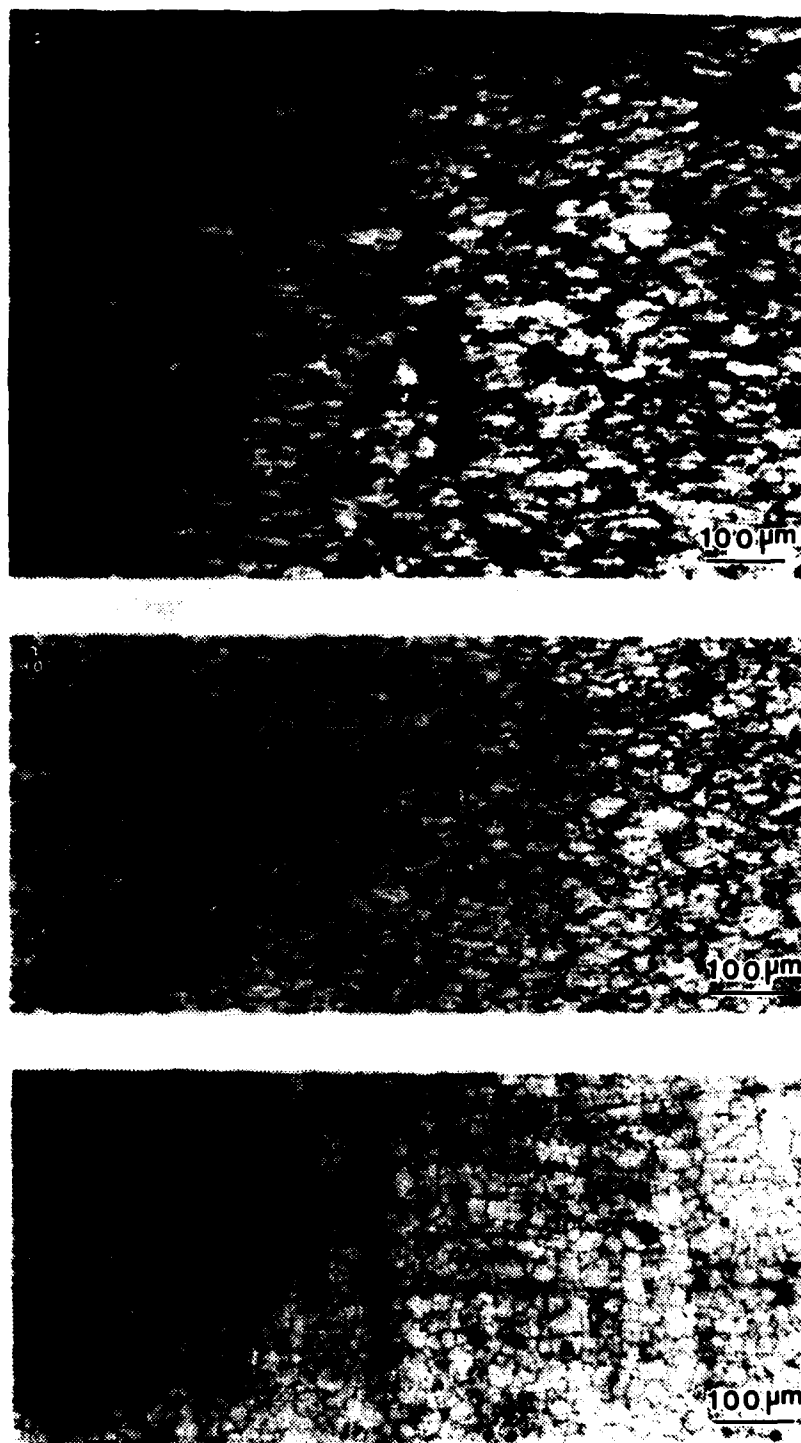


Figure 4.30 Optical micrographs of a recrystallized test specimen deformed at 300°C and $\dot{\epsilon} = 6.67 \times 10^{-3} \text{s}^{-1}$: (a) fracture point, (b) gage section and (c) grip section.

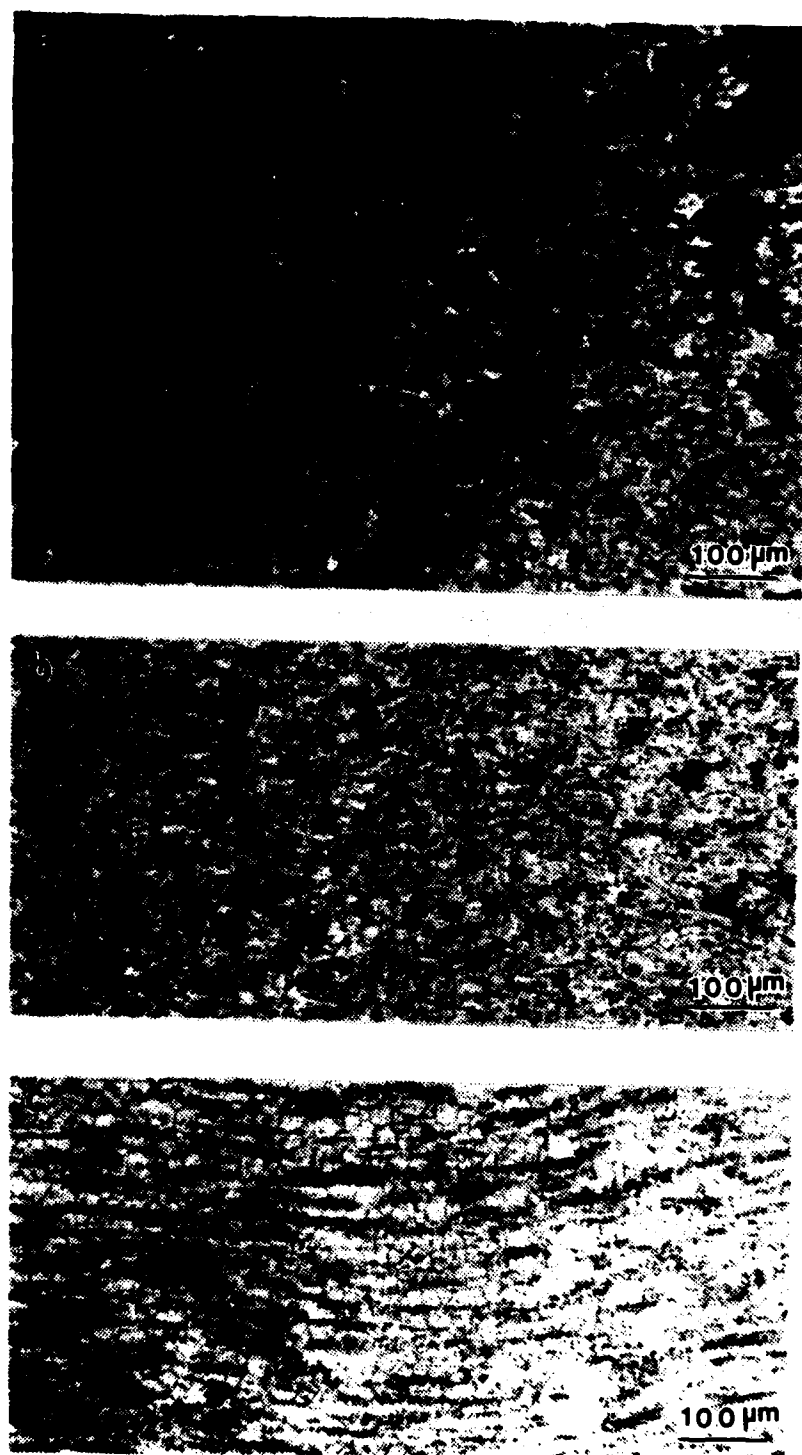


Figure 4.31 Optical micrographs of a recrystallized test specimen deformed at 300°C and $\dot{\epsilon} = 6.67 \times 10^{-4} \text{ s}^{-1}$: (a) fracture point, (b) gage section and (c) grip section.

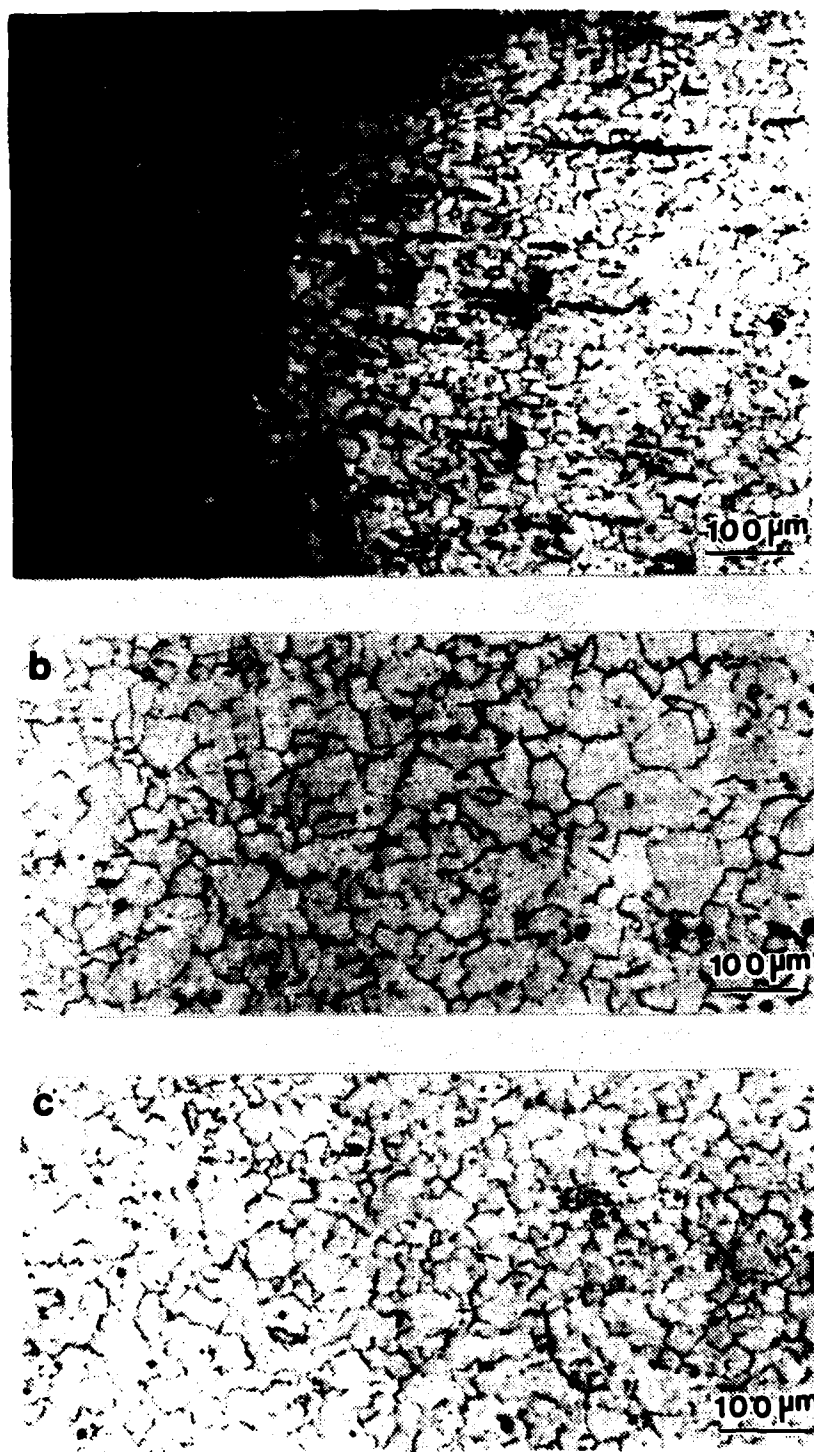


Figure 4.32 Optical micrographs of a recrystallized test specimen deformed at 400°C and $\dot{\epsilon} = 6.67 \times 10^{-2} \text{s}^{-1}$: (a) fracture point, (b) gage section and (c) grip section.

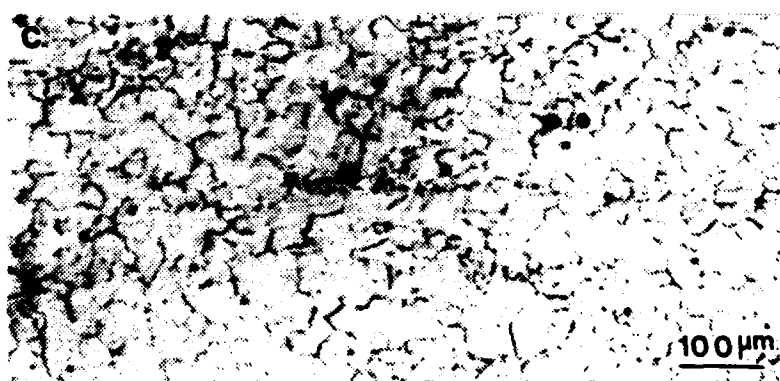
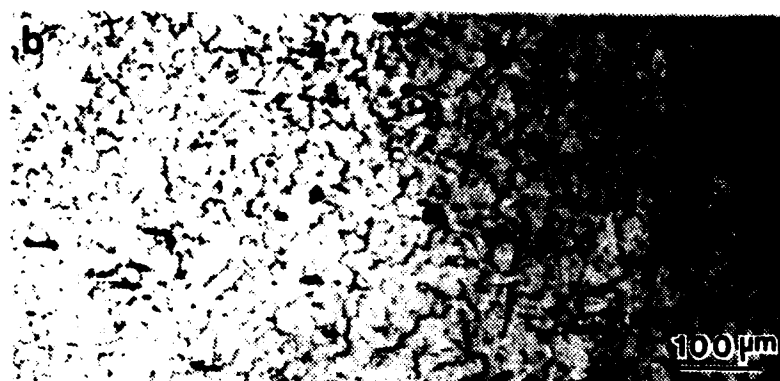


Figure 4.33 Optical micrographs of a recrystallized test specimen deformed at 400°C and $\dot{\epsilon} = 6.67 \times 10^{-3} \text{ s}^{-1}$: (a) fracture point, (b) gage section and (c) grip section.

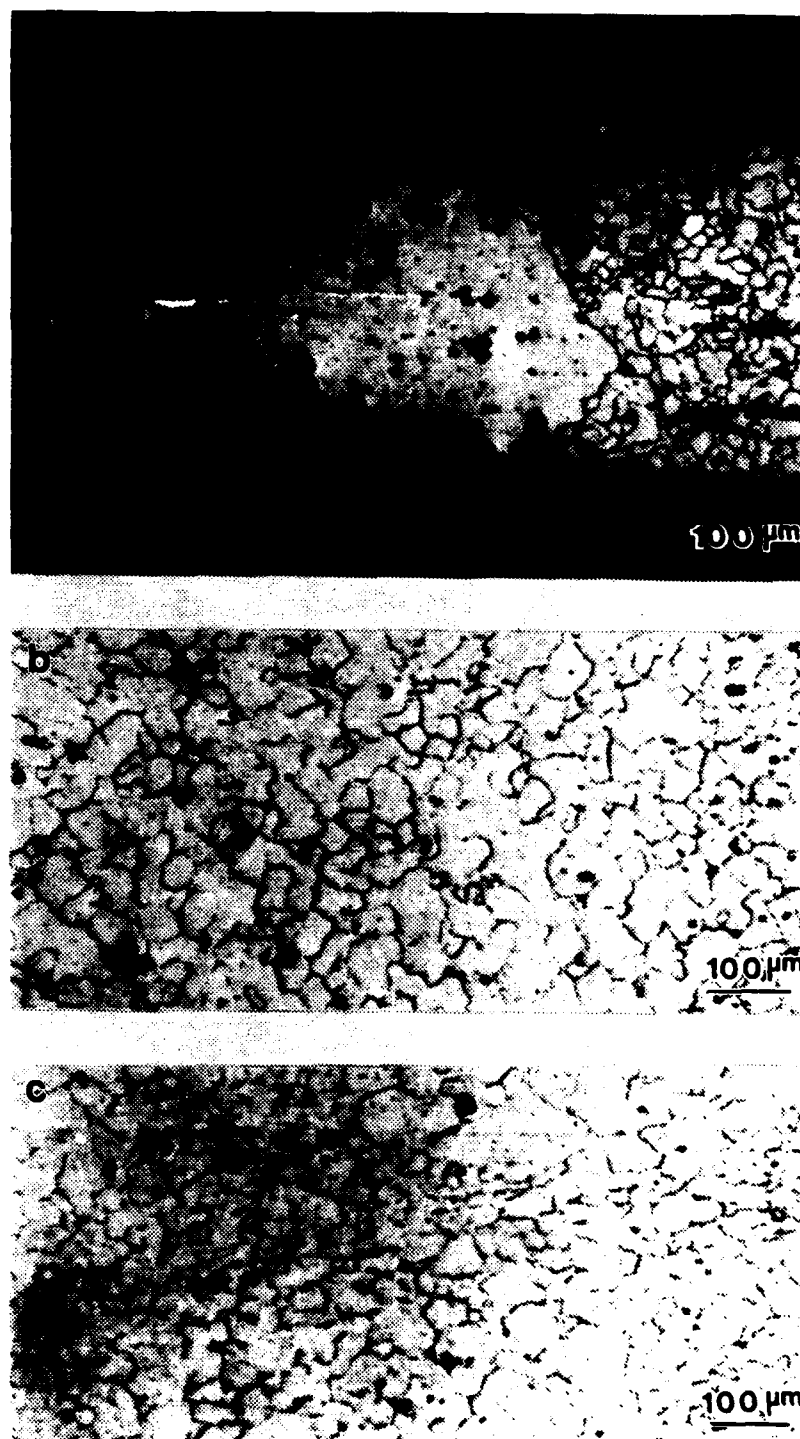


Figure 4.34 Optical micrographs of a recrystallized test specimen deformed at 400°C and $\dot{\epsilon} = 6.67 \times 10^{-4} \text{ s}^{-1}$: (a) fracture point, (b) gage section and (c) grip section.

extent of grain growth. The difference in grain size in turn is attributed to the as-rolled specimen having to undergo recovery and recrystallization before grain growth occurs whereas the recrystallized specimen only undergoes grain growth upon heating to the 400°C test temperature.

D. MICROSTRUCTURAL EXAMINATION OF ANNEALED TEST SPECIMENS

1. Annealed Treatment

An annealing treatment, intended to induce recovery, not recrystallization, was adopted in this research to determine if such a recovered and stabilized microstructure might enhance superplasticity at warm (i.e., 300°C) temperatures. The principal microstructural change during recovery is the rearrangement of dislocations to a more stable configuration. This leads to a reduction in the macro- and microstresses associated with a worked piece. An annealing time at 200°C was determined by exposing as-rolled specimens to 1 hour, 5 hour and 10 hour periods of annealing and then examining the microstructural differences. As illustrated in Figure 4.35 little microstructural changes take place after 1 hour of annealing. Hence, an annealing treatment of 1 hour at 200°C was used.

2. Specimens Tested at 300°C

These specimens, and others tested at a temperature below the solvus, showed an increase in superplastic elongations as the strain rate was decreased. As

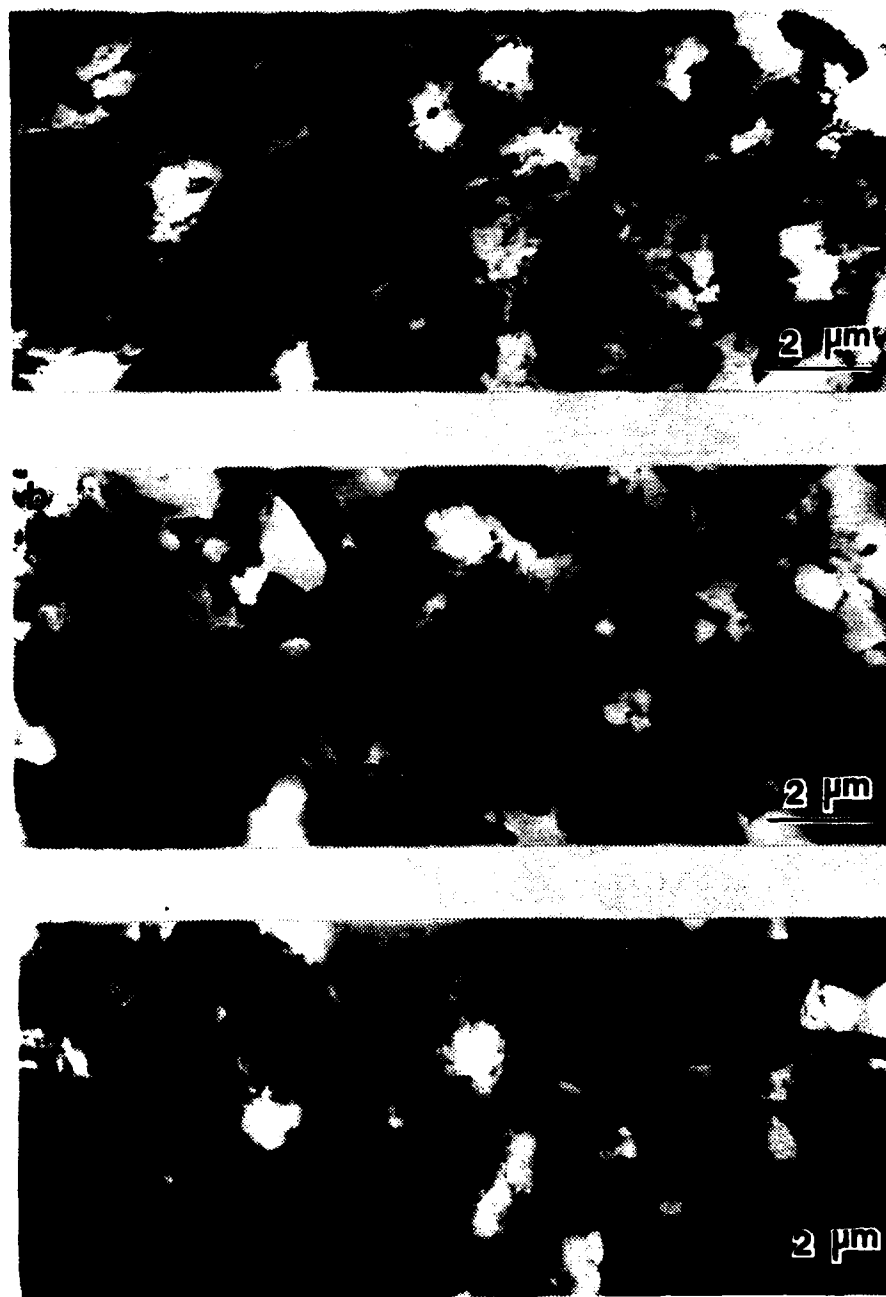


Figure 4.35 TEM micrographs of Al-10%Mg-0.1%Zr alloy in the warm rolled condition annealed at 200°C for times: (a) as-rolled, (b) 1 hour and (c) 10 hours.

illustrated in Figure 4.36 the slower strain rate test resulted in an apparently well organized, high-angle grain structure. From this observation it is concluded that complete dynamic recrystallization has occurred. In comparison with previous work by Stengel [Ref. 11], however, this annealing was not as effective. Stengel reported enhanced ductility at all strain rates where here ductility enhancement was found only at low strain rates. The reason may be related to the previously reported observation of non-uniform zirconium distribution.

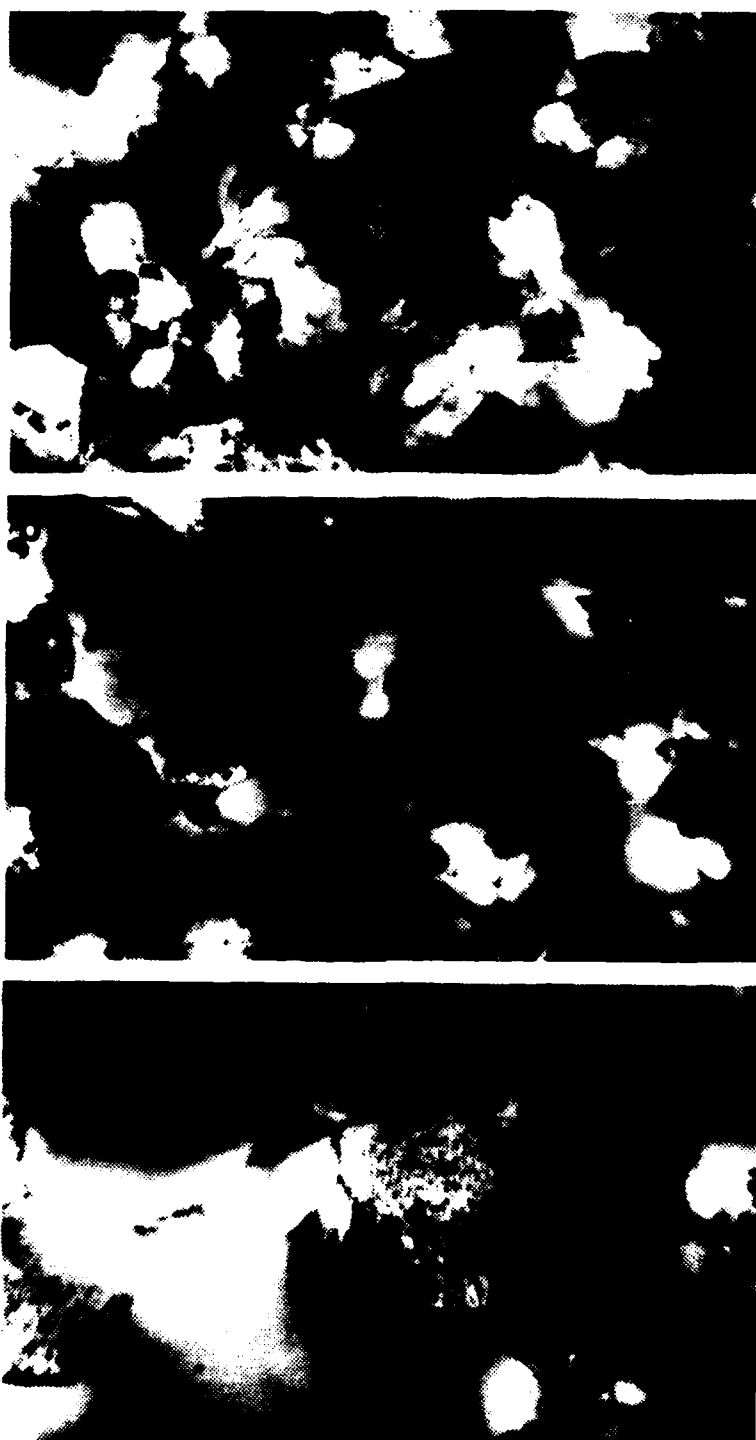


Figure 4.36 TEM micrographs of annealed test specimens deformed to fracture at 300°C: (a) $\dot{\epsilon} = 6.67 \times 10^{-3} \text{ s}^{-1}$, (b) $\dot{\epsilon} = 6.67 \times 10^{-4} \text{ s}^{-1}$, and (c) $\dot{\epsilon} = 6.67 \times 10^{-5} \text{ s}^{-1}$.

V. CONCLUSION AND RECOMMENDATION

The following conclusions are drawn from this research:

- 1) zirconium addition, even as low as 0.1 percent, is not kept in solution during commercial chill-casting of a 10%Mg aluminum magnesium alloy;
- 2) the thermomechanical processing scheme followed in this research results in a homogeneous microstructure;
- 3) warm temperature (i.e., 300°C) superplastic deformation of a specimen in the as-rolled condition results in a dynamically recrystallized microstructure with negligible cavitation;
- 4) regardless of test specimen microstructural condition, above the solvus tensile testing results in a recrystallized, high-angle boundary, grain structure with extensive cavitation present;
- 5) large particles (i.e., ZrAl_3) act as initiation sites for cavitation formation.

Continued research in the following areas is recommended:

- 1) Study the effects that magnesium content has on zirconium solubility;
- 2) Investigate casting methods that might retain zirconium in solution, that typical chill-casting is unable to accomplish;
- 3) Investigate strength and corrosion resistance of the as-rolled material after deformation;
- 4) study of cavitation initiation and growth via optical examination of specimens exposed to various

strains; 5) further investigation into annealing treatments that might optimize superplastic properties.

LIST OF REFERENCES

1. Ness, F. G., Jr., High Strength to Weight Aluminum-13 Weight Percent Magnesium Alloy Through Thermomechanical Processing, M.S. Thesis, Naval Postgraduate School, Monterey, California, December 1976.
2. Bingay, C. P., Microstructural Response of Aluminum-Magnesium Alloys to Thermomechanical Processing, M.S. Thesis, Naval Postgraduate School, Monterey, California, December 1977.
3. Glover, T. L., Effects of Thermomechanical Processing of Aluminum-Magnesium Alloys Containing High Weight Percent Magnesium, M.S. Thesis, Naval Postgraduate School, Monterey, California, December 1977.
4. Grandon, R. A., High Strength Aluminum-Magnesium Alloys: Thermomechanical Processing, Microstructure and Tensile Mechanical Properties of High Strength Aluminum-Magnesium Alloys, M.S. Thesis, Naval Postgraduate School, Monterey, California, March 1980.
5. Speed, W. G., An Investigation into the Influence of Thermomechanical Processing on Microstructure and Mechanical Properties of High Strength Aluminum-Magnesium Alloys, M.S. Thesis, Naval Postgraduate School, Monterey, California, December 1977.
6. Chesterman, C. W., Jr., Precipitation, Recovery and Recrystallization Under Static and Dynamic Conditions for High Magnesium Aluminum-Magnesium Alloys, M.S. Thesis, Naval Postgraduate School, Monterey, California, March 1980.
7. Johnson, R. B., The Influence of Alloy Composition and Thermomechanical Processing Procedure on Microstructural and Mechanical Properties of High Magnesium Aluminum-Magnesium Alloys, M.S. Thesis, Naval Postgraduate School, Monterey, California, June 1980.
8. Shirah, R. J., The Influence of Solution Time and Quench Rate on the Microstructure and Mechanical Properties of High Magnesium Aluminum-Magnesium Alloys, M.S. Thesis, Naval Postgraduate School, Monterey, California, December 1981.

9. Becker, J. J., Superplasticity in Thermomechanically Processed High-Magnesium Aluminum Magnesium Alloys, M.S. Thesis, Naval Postgraduate School, Monterey, California, March 1984.
10. Mills, M. E., Superplasticity in Thermomechanically Processed Aluminum-10.2%Mg-0.52%Mn Alloy, M.S. Thesis, Naval Postgraduate School, Monterey, California, September 1984.
11. Stengel, A. R., Effects of Annealing Treatments on Superplasticity in a Thermomechanically Processed Aluminum-10.2%Mg-0.52%Mn Alloy, M.S. Thesis, Naval Postgraduate School, Monterey, California, December 1984.
12. Self, R. J., The Effect of Alloy Additions on Superplasticity in Thermomechanically Processed High Magnesium Aluminum Magnesium Alloys, M.S. Thesis, Naval Postgraduate School, Monterey, California, December 1984.
13. Lloyd, D. J. and Moore, D. M., "Aluminum Alloy Design for Superplasticity," Superplastic Forming of Structure Alloys, Conference Proceedings of TMS-AIME, pp. 147-172, June 1982.
14. Underwood, L. F., "A Review of Superplasticity and Related Phenomena," Journal of Metals, pp. 914-919, 1962.
15. Stengall, M. J., "Cavitation in Superplasticity," Superplastic Forming of Structure Alloys, Conference Proceedings of TMS-AIME, pp. 321-336, June 1982.
16. Nabarro, F. R. M., Report of a Conference on the Strength of Solids, Physical Society (Publishers), London, p. 75, 1948.
17. Herring, C., "Diffusional Viscosity of A Polycrystalline Solid," Journal Applied Physics, Volume 21, p. 437, 1950.
18. Coble, R. L., "A Model for Boundary Diffusion Controlled Creep in Polycrystalline Materials," Journal Applied Physics, Volume 34, p. 1679, 1963.
19. Ashby, M. F., "A First Report on Deformation-Mechanism Maps," Acta Metallurgica, Volume 20, p. 887, 1972.

20. Ashby, M. F. and Verrall, R. A., "Diffusion-Accommodated Flow and Superplasticity," Acta Metallurgica, Volume 21, pp. 149-163, 1973.
21. Weertman, J., "Dislocation Climb Theory of Steady-State Creep," Transactions of the ASM, Volume 61, p. 681, 1968.
22. Sherby, O. D. and Burke, P. M., "Mechanical Behavior of Crystalline Solids at Elevated Temperatures," Progress in Materials Science, Volume 13, p. 325, 1968.
23. Hamilton, C. H., Bampton, C. C., and Patton, N. E., "Superplasticity in High Strength Aluminum Alloys," Superplastic Forming of Structure Alloys, Conference Proceedings of TMS-AIME, pp. 173-189, June 1982.
24. Patton, N. E., Hamilton, D. H., Wert, J., and Mahoney, M., "Characterization of Fine-Grained Superplastic Aluminum Alloys," Journal of Metals, pp. 21-27, August 1982.
25. Wert, J. A., "Grain Refinement and Grain Size Control," Superplastic Forming of Structure Alloys, Conference Proceedings of TMS-AIME, pp. 69-83, June 1982.
26. Bly, D. C., Sherby, O. D., and Young, C. M., Influence of Thermal Mechanical Treatments on the Mechanical Properties of a Finely Spheroidized Eutectic Composition Steel," Material Science and Engineering, Volume 2, pp. 41-46, 1973.
27. Alcoa Technical Center, Ltr, August 1984.
28. Hartmann, T. S., Mechanical Characteristics of a Superplastic Aluminum-10%Mg-0.1%Zr Alloy, M.S. Thesis, Naval Postgraduate School, Monterey, California, June 1985.
29. Alcamo, M.E., Effects of Strain and Strain Rate on the Microstructure of a Superplastically Deformed Al-10%Mg-0.1%Zr Alloy, M.S. Thesis, Naval Postgraduate School, Monterey, California, June 1985.
30. Mondolfo, L. F., Aluminum Alloys, Structure and Properties, Butterworths, London, 1976, p. 590.
31. McNelley, T. R. and Garg, A., "Development of Structure and Mechanical Properties in Al-10.2%Mg by Thermomechanical Processing," Scripta Metallurgical, Volume 18, pp. 917-920, 1984.

INITIAL DISTRIBUTION LIST

	<u>No. Copies</u>
1. Defense Technical Information Center Cameron Station Alexandria, Virginia 22304-6145	2
2. Library, Code 0142 Naval Postgraduate School Monterey, California 93943-5100	2
3. Department Chairman, Code 69Mx Department of Mechanical Engineering Naval Postgraduate School Monterey, California 93943-5100	1
4. Professor T. R. McNelley, Code 69Mc Department of Mechanical Engineering Naval Postgraduate School Monterey, California 93943-5100	5
5. Mr. Richard Schmidt, Code AIR 320A Naval Air Systems Command Naval Air Systems Command Headquarters Washington, D.C. 20361	1
6. Dr. Eu Whee Lee Naval Air Development Center Materials Science Department Warminster, Pennsylvania 18974	1
7. LT Dudley B. Berthold, USN Nuclear Power School Naval Training Center Orlando, Florida 32813	5

END

FILMED

11-85

DTIC